Published for SISSA by Springer

Received: *February 14, 2022*
Revised: *April 11, 2022*
Accepted: *April 29, 2022*
Published: *May 27, 2022*

Secluded dark matter in gauged $B - L$ model

Priyotosh Bandyopadhyay,[a] Manimala Mitra,[c,d] Rojalin Padhan,[c,d] Abhishek Roy[c,d] and Michael Spannowsky[b]

[a] *Indian Institute of Technology Hyderabad, Kandi, Sangareddy-50228, Telengana, India*

[b] *Institute for Particle Physics Phenomenology, Department of Physics, Durham University, South Road, Durham DH1 3LE, U.K.*

[c] *Institute of Physics, Sachivalaya Marg, Bhubaneswar, Pin-751005, Odisha, India*

[d] *Homi Bhabha National Institute, BARC Training School Complex, Anushakti Nagar, Mumbai 400094, India*

E-mail: bpriyo@phy.iith.ac.in, manimala@iopb.res.in, rojalin.p@iopb.res.in, abhishek.r@iopb.res.in, michael.spannowsky@durham.ac.uk

Abstract: We consider the gauged $B - L$ model which is extended with a secluded dark sector, comprising of two dark sector particles. In this framework the lightest $\mathcal{Z}_2$-odd particle is the dark matter candidate, having a feeble interaction with all other SM and BSM states. The next-to-lightest $\mathcal{Z}_2$-odd particle in the dark sector is a super-wimp, with large interaction strength with the SM and BSM states. We analyse all the relevant production processes that contribute to the dark matter relic abundance, and broadly classify them in two different scenarios, a) dark matter is primarily produced via the non-thermal production process, b) dark matter is produced mostly from the late decay of the next-to-lightest $\mathcal{Z}_2$-odd particle. We discuss the dependency of the relic abundance of the dark matter on various model parameters. Furthermore, we also analyse the discovery prospect of the BSM Higgs via invisible Higgs decay searches.

Keywords: Models for Dark Matter, Particle Nature of Dark Matter, Dark Matter at Colliders

ArXiv ePrint: 2201.09203

https://doi.org/10.1007/JHEP05(2022)182

Contents

1 Introduction

Observational evidence shows that 84% matter of the universe is in the form of non-baryonic dark matter. However, very little is known about the nature of dark matter (DM) and its origin. The Standard Model (SM) can not explain the observed relic density. One of the most favoured scenarios for DM production has been thermal freeze-out, where a weakly interacting massive particle (WIMP) serves as a DM candidate. The WIMP with electroweak-scale mass, which interacts with other particles via electroweak interaction, can naturally explain the measured DM relic density of $\Omega h^2 = 0.1199 \pm 0.0027$ [1]. Several direct detection experiments so far have searched for a WIMP. However, the lack of conclusive experimental evidence motivates the exploration of alternate dark matter production mechanisms. The production of DM via freeze-in mechanism [2–10] is one of the most popular production mechanisms. In this framework, DM has a very tiny interaction with the SM and any other particle which are in thermal equilibrium with the plasma and thereby referred to as feebly interacting massive particle (FIMP). Due to significantly suppressed interaction with SM/BSM particles, the FIMP DM never attains thermal equilibrium. Due to a similar suppression in the interaction with the SM particles, FIMP, in general, can

JHEP05(2022)182

not produce any observable signal in the direct detection experiments. See [11] for other alternatives with a light mediator. The DM in the freeze-in scenario is produced from the decay and/or annihilation of SM, and BSM particles which are either in equilibrium with the thermal plasma or also freezing-in along with the DM [12].

Apart from the DM abundance, the SM fails to explain neutrino masses and mixings. One of the most promising models that explain small neutrino masses is the gauged $B-L$ model, which contains three right-handed neutrinos (RHNs) [13–16] that generate light neutrino masses via seesaw mechanism [17, 18]. In addition, the model also contains one BSM gauge boson Z_{BL} and a complex scalar field S. The scalar field acquires vacuum expectation value and breaks the $B-L$ gauge symmetry. The BSM gauge boson and the heavy neutrinos acquire their masses due to the spontaneous breaking of the $B-L$ gauge symmetry. The model can further be extended with a secluded dark sector with a scalar particle ϕ_D with non-zero $B-L$ charge and a gauge singlet fermion state χ, where either or both of them can be suitable DM candidates. The dark sector particles are odd under a $\mathcal{Z}_2$ symmetry. The thermal DM for this model has been explored in several works, such as [19, 20]. For a different variation of the $B-L$ gauge model with only a thermal scalar DM, see [21–25]. For RHN DM in a typical $B-L$ model, see [26–31]. The RHN can also serve as a portal between the SM sector and a secluded dark sector containing DM particles, see [32–34] for the relevant discussion. One of the interesting possibilities is if the fermion state χ serves as the non-thermal DM candidate, and the scalar particle ϕ_D, which was in thermal equilibrium in the early universe, has a significant contribution in the production of χ.

In this article, we consider this possibility, where χ is the DM state, and ϕ_D significantly impacts its production. We study the production of DM through a thermal freeze-in mechanism and significant non-thermal freeze-in contribution [3, 35] from the decay of ϕ_D. The state χ interacts only with ϕ_D and RHN N. The DM candidate χ never thermalises due to very tiny coupling. This work considers that ϕ_D is heavier than χ state. However, it serves as the next-to-lightest $\mathcal{Z}_2$-odd particle (NLOP). ϕ_D thermalises with the SM particles because of large quartic couplings in the scalar potential, sizeable SM-BSM Higgs mixing angle, and large gauge coupling. DM is primarily produced at high temperatures via a thermal freeze-in mechanism from the decay of bath particle ϕ_D, which was in equilibrium with the rest of the plasma. ϕ_D subsequently decoupled from the thermal bath, and its late decay further produced substantial DM relic density. The abundance of ϕ_D at the time of decoupling $\Omega^{FO}_{\phi_D}h^2$ is governed by the freeze-out mechanism. Depending upon the abundance $\Omega^{FO}_{\phi_D}h^2$ and its conversion to χ state through out-of-equilibrium decay, the DM can primarily be produced from the late decay as well, which we refer as non-thermal production of DM. We divide the discussion into two different scenarios and show the importance of thermal and non-thermal freeze-in contributions in determining DM relic abundance. We elaborately discuss the constrain on other model parameters, such as the scalar quartic couplings, SM-BSM Higgs mixing angle and the mass of ϕ_D and χ, that appear from the relic density constraint. Other than this, we also explore the discovery prospect of this model at the future High Luminosity run of the LHC (HL-LHC), mainly focusing on the heavy Higgs searches. Due to non-zero coupling λ_{SD} between the state ϕ_D

	h	N	L	Q	u_R	d_R	e_R	S	ϕ_D	χ
Y_{B-L}	0	-1	-1	1/3	1/3	1/3	1	2	1	0
$\mathcal{Z}_2$	1	1	1	1	1	1	1	1	-1	-1

Table 1. Charges of all the particles under $B-L$ and $\mathcal{Z}_2$ symmetry.

and $B-L$ Higgs S, the model offers a largely invisible branching ratio of the BSM Higgs state. We analyse the discovery potential of the BSM Higgs H_2-ϕ_D scalar quartic coupling at the HL-LHC in vector-boson fusion (VBF) channel. This quartic coupling has a large impact in determining ϕ_D abundance, hence the DM relic density.

The paper is organised as follows. In section 2, we describe the model. Following this in section 3, we discuss the dark matter production in detail and along with the effect of out-of-equilibrium decay of ϕ_D. And later, we discuss the collider prospects on the search of ϕ_D at the LHC in section 4. We present our conclusion in section 5. In appendix A.1, A.2 and A.3, we provide the necessary calculation details.

2 Model

The model is a gauged $B-L$ model, augmented with a secluded dark sector. In addition to the particles of the gauged $B-L$ model, i.e., the right-handed neutrinos N, BSM Higgs field S and BSM gauge boson Z_{BL}, the model also contains dark sector particles a complex scalar state ϕ_D and a $B-L$ singlet fermion χ. The dark sector particles are odd under $\mathcal{Z}_2$ symmetry, while other particles are even. The $\mathcal{Z}_2$ symmetry ensures the stability of DM. We consider that the BSM sector of the gauged $B-L$ model and the SM Higgs state h act as a portal between other SM particles and the dark sector.[1]

The charge assignments of different particles are shown in table 1. Here, the field S represents a complex scalar field, which acquires vacuum expectation value (vev) $v_{BL} \neq 0$ and breaks $B-L$ gauge symmetry. The state N contributes to the light neutrino mass generation via the seesaw mechanism. Note that the scalar ϕ_D is non-trivially charged under $B-L$ gauge symmetry, while the fermion χ is a singlet under both the $B-L$ and SM gauge group. As we will see in the subsequent sections, this leads to significant differences in the evolution of χ and ϕ_D abundances. The complete Lagrangian of the model has the following form,

$$\mathcal{L} = \mathcal{L}_{SM} + \mathcal{L}_{DM} + \mathcal{L}_{B-L}, \tag{2.1}$$

where $\mathcal{L}_{DM}$ is the Lagrangian containing dark sector particles, and $\mathcal{L}_{B-L}$ is the $B-L$ Lagrangian. The $B-L$ Lagrangian has the following form,

$$\begin{aligned}\mathcal{L}_{B-L} = {}& (D_\mu S)^\dagger (D^\mu S) - \frac{1}{4} F_{BL\mu\nu} F^{\mu\nu}_{BL} + i\bar{N}_i \gamma^\mu D_\mu N_i - V_{B-L}(h,S) \\ & - \sum_{i=1}^{3} \lambda_{NS} S \bar{N}_i^c N_i - \sum_{i,j=1}^{3} y'_{N,ij} \bar{L}_i \tilde{h} N_j + \text{h.c.}\ ,\end{aligned} \tag{2.2}$$

$$V_{B-L}(h,S) = \mu_S^2 S^\dagger S + \mu_h^2 h^\dagger h + \lambda_S \left(S^\dagger S\right)^2 + \lambda_h \left(h^\dagger h\right)^2 + \lambda_{Sh} \left(h^\dagger h\right)\left(S^\dagger S\right),$$

[1]In our notation, h represents the SM Higgs doublet field.

The dark sector Lagrangian is given by,

$$\mathcal{L}_{DM} = \bar{\chi}(i\not{\partial} - m_\chi)\chi + (D^\mu \phi_D)^\dagger (D_\mu \phi_D) - \mu_D^2 \left(\phi_D^\dagger \phi_D\right) - \lambda_D \left(\phi_D^\dagger \phi_D\right)^2 \\ - \lambda_{Dh} \left(\phi_D^\dagger \phi_D\right)\left(h^\dagger h\right) - \lambda_{SD}\left(\phi_D^\dagger \phi_D\right)\left(S^\dagger S\right) - (Y_{D\chi}\bar{\chi}\phi_D N + \text{h.c.})\,. \tag{2.3}$$

The interaction strength between ϕ_D and BSM and SM Higgs bosons (i.e, S and h) are proportional to λ_{SD} and λ_{Dh}. The kinetic energy terms involving S, ϕ_D and N contains the covariant derivatives which is given by,

$$D_\mu X = (\partial_\mu + i g_{BL} Y_{B-L}(X) Z_{BL\mu})X, \tag{2.4}$$

where $X = S,\ N,\ \phi_D$ and $Y_{B-L}(X)$ represents $B-L$ charge of the states shown table 1.

- *SM Higgs and BSM Higgs*: after spontaneous symmetry breaking (SSB), the SM Higgs doublet h and BSM scalar S is given by,

$$h = \begin{pmatrix} 0 \\ \dfrac{v+h_1}{\sqrt{2}} \end{pmatrix} \quad S = \left(\frac{v_{BL}+h_2}{\sqrt{2}}\right). \tag{2.5}$$

  Owing to the non-zero λ_{Sh}, h_1 and h_2 mixes with each other which leads to the scalar mass matrix given by,

$$\mathcal{M}^2_{\text{scalar}} = \begin{pmatrix} 2\lambda_h v^2 & \lambda_{Sh}\, v_{BL}\, v \\ \lambda_{Sh}\, v_{BL}\, v & 2\lambda_S v_{BL}^2 \end{pmatrix}. \tag{2.6}$$

  The basis states h_1 and h_2 can be rotated by suitable angle θ to the new basis states H_1 and H_2. The new basis states represents the physical basis states which are given by,

$$H_1 = h_1 \cos\theta - h_2 \sin\theta, \tag{2.7}$$

$$H_2 = h_1 \sin\theta + h_2 \cos\theta, \tag{2.8}$$

  where H_1 is the SM like Higgs and H_2 is the BSM Higgs. The mixing angle between the two states is defined by,

$$\tan 2\theta = \frac{v v_{BL} \lambda_{Sh}}{v^2 \lambda_h - v_{BL}^2 \lambda_S}. \tag{2.9}$$

  The mass square eigenvalues of H_1 and H_2 are given by,

$$M^2_{H_1,H_2} = \lambda_h v^2 + \lambda_S v_{BL}^2 \pm \sqrt{(\lambda_h v^2 - \lambda_S v_{BL}^2)^2 + (\lambda_{Sh} v v_{BL})^2}. \tag{2.10}$$

- *Neutrino mass*: the Majorana mass term of RHN's is generated through spontaneous symmetry breaking of $B-L$ symmetry. The mass of RHN's is given by,

$$M_N = \frac{\lambda_{NS}\ v_{BL}}{\sqrt{2}}. \tag{2.11}$$

JHEP05(2022)182

The mass of the SM neutrinos is generated through Type-I seesaw mechanism where the light neutrino mass matrix has the following expression,

$$m^{\nu}_{ij} = \frac{y'_{N,ik} y'_{N,kj} \langle h \rangle^2}{M_{N,k}}. \tag{2.12}$$

- *Gauge boson mass*: similar to the RHN's, the additional neutral gauge boson mass $Z_{\rm BL}$ is generated via spontaneous breaking of $B-L$ gauge symmetry. The mass of $Z_{\rm BL}$ is related to the symmetry breaking scale v_{BL} as,

  $$M_{Z_{\rm BL}} = 2 g_{BL} v_{BL}, \tag{2.13}$$

  where g_{BL} is the associated $B-L$ gauge coupling constant.

- *Dark sector constituents mass*: she mass square of the particle ϕ_D has the following form,

  $$m^2_{\phi_D} = \mu_D^2 + \frac{\lambda_{Dh} v^2}{2} + \frac{\lambda_{SD} v_{BL}^2}{2}. \tag{2.14}$$

  Note that, both electroweak symmetry breaking vev v and the $B-L$ symmetry breaking vev v_{BL} have impact in determining the mass of ϕ_D. In this work, we consider λ_{SD} and λ_{Dh} in between 10^{-1} and 10^{-5} to have ϕ_D as the thermal particle.

- The DM candidate χ is singlet under SM and $B-L$ gauge group. It's mass is governed by the bare mass term, i.e., m_χ.

3 Dark matter

The dark sector fields χ and ϕ_D can be DM particles. However, we consider the scenario, where χ is a non-thermal FIMP DM, and ϕ_D, the NLOP, is primarily responsible for DM production. In the early universe, the state ϕ_D was in thermal equilibrium with the bath particles, and at some later epoch denoted as T_d, it decoupled from the rest of the plasma. Other than the standard thermal freeze-in contribution via $\phi_D \to \chi N$ process effective up to epoch $T \sim m_{\phi_D} > T_d$, the out-of-equilibrium decay of ϕ_D into χ also contributes significantly in the relic abundance of DM. Below, we explore this possibility in detail.

3.1 Super-WIMP ϕ_D+ FIMP DM χ

This is to note that the particle χ has only one portal interaction $Y_{D\chi}\bar{\chi}\phi_D N$ with the dark sector field ϕ_D and the RHN field N, where $Y_{D\chi}$ is the respective coupling. We consider $Y_{D\chi} \sim \mathcal{O}(10^{-10}$–$10^{-12})$ to be very small, and hence, χ has feeble interaction with every other particle of this model. Due to tiny interaction, it fails to thermalise with the rest of the plasma. It was produced from the decay and annihilation of the SM and BSM particles in the early epoch. We show Feynman diagram for all possible decay and annihilation processes that contribute to the χ production in figure 1. Among all these processes, the production of χ from decay processes, however, dominates. The sub-dominant contribution to the production of χ from the annihilation of SM and BSM states

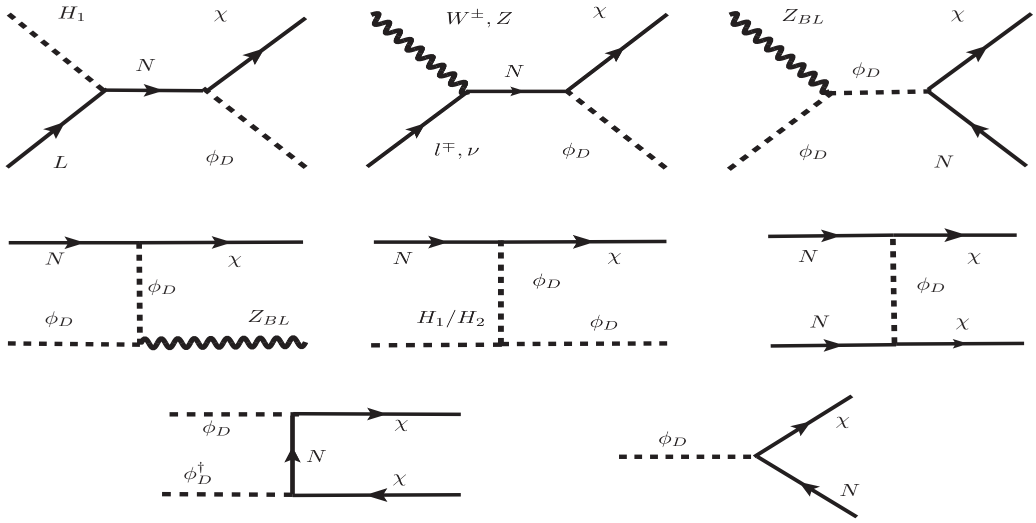

Figure 1. Different contributions for the production of the DM χ. The s and t channels diagrams give negligible contributions compared to the decay process.

arises due to additional small couplings, heavy propagators, and suppression factors arising from phase space integral.

This work sticks to the renormalizable interaction between the dark sector, the SM, and $B-L$ particles. Therefore, the production of χ is insensitive to the reheating temperature, set by reheating/end of inflationary dynamics. The abundance of χ builds up primarily due to the $\phi_D \to \chi N$ process and increases when $T > m_{\phi_D}$. The production of χ is most significant when $T \approx m_{\phi_D}$. When the temperature falls below m_{ϕ_D}, i.e., $T < m_{\phi_D}$, Boltzmann suppression of the parent state ϕ_D occurs and DM χ freezes in. This is referred to as thermal freeze-in production, as the parent particle ϕ_D during this epoch has been in thermal equilibrium. In addition to the standard thermal freeze-in contribution, the abundance of DM χ can further be enhanced from the out-of-equilibrium decay of ϕ_D. This occurs at a later epoch $T \ll m_{\phi_D}$, when ϕ_D is in out-of-equilibrium. The production of DM from the late decay of a state which has decoupled from the thermal plasma is referred to as the super-wimp mechanism, which has been discussed in [3, 35–38]. In our scenario, the state ϕ_D serves as a super-wimp candidate.

The state ϕ_D having non-zero $B-L$ charges and non-zero quartic couplings λ_{SD} and λ_{Dh} interacts abundantly with the SM and $B-L$ particles. At an earlier epoch, ϕ_D hence was in thermal equilibrium with surrounding plasma, maintaining an equilibrium distribution. The non-thermal decay of ϕ_D, which enhances the DM relic density, takes place at a late stage in the thermal history. The dark sector state ϕ_D tracked equilibrium abundance when the temperature of the universe was greater than its mass. The dark sector states ϕ_D abundance decreases mainly through annihilation which are efficient up until $\frac{m_{\phi_D}}{T} \approx 25$. Feynman diagram for ϕ_D depletion through annihilation to B/SM particles is shown in figure 2. Around this temperature, the interaction rate for the annihilation/scattering of ϕ_D becomes less than the expansion rate of the universe. Hence, ϕ_D fails to scatter with surrounding plasma constituents, and it decouples from the cosmic soup.

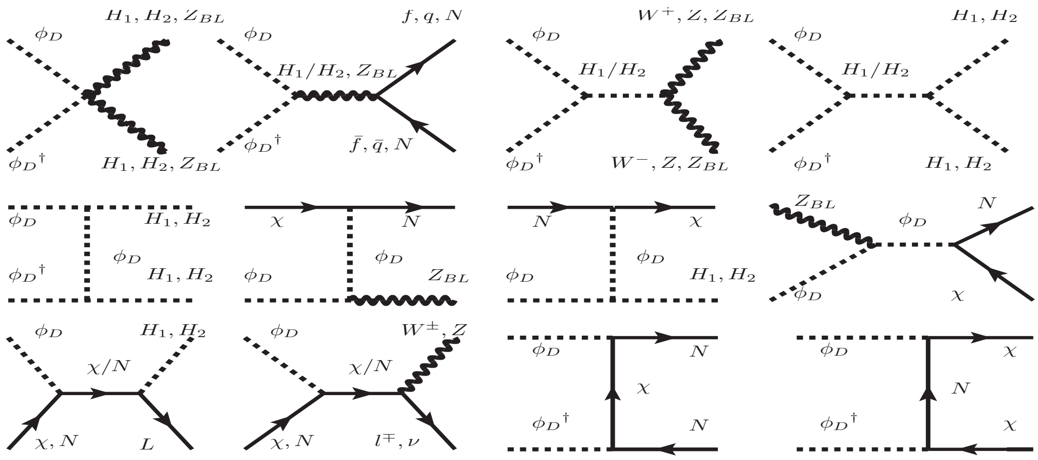

Figure 2. Annihilation/scattering channels of ϕ_D.

To compute the relic density of dark sector constituents, one needs to study the evolution of the number density of its constituents with the temperature of the universe. The evolution of the number density of the dark sector constituents is governed by the Boltzmann equations, which contain all the information of the number changing processes of the dark sector constituents. The Boltzmann equations for the evolution of ϕ_D and χ in terms of its co-moving number density $Y_{\phi_D/\chi} = n_{\phi_D/\chi}/s$, where $n_{\phi_D/\chi}$ and s are the actual number density of ϕ_D and χ and entropy density of the universe are given by,

$$\begin{aligned}
\frac{dY_{\phi_D}}{dx} = &\frac{1}{x^2}\frac{s(m_{\phi_D})}{H(m_{\phi_D})}\Bigg[\sum_{i,j=1}^{2}\left(\delta_{ij}+\frac{1}{2}|\epsilon_{ij}|\right)\langle\sigma v\rangle_{\phi_D^\dagger\phi_D\to H_iH_j}({Y^{eq}_{\phi_D}}^2 - Y^2_{\phi_D}) \\
&+\langle\sigma v\rangle_{\phi_D^\dagger\phi_D\to W^+W^-}({Y^{eq}_{\phi_D}}^2 - Y^2_{\phi_D}) + \langle\sigma v\rangle_{\phi_D^\dagger\phi_D\to ZZ}({Y^{eq}_{\phi_D}}^2 - Y^2_{\phi_D}) \\
&+\sum_{X=H_i,Z_{BL}}\langle\sigma v\rangle_{\phi_D\chi\to NX}(Y^{eq}_{\phi_D}Y^{eq}_{\chi} - Y_{\phi_D}Y_\chi) + \sum_{f=N,t,b}\langle\sigma v\rangle_{\phi_D^\dagger\phi_D\to f\bar{f}}({Y^{eq}_{\phi_D}}^2 - Y^2_{\phi_D})\Bigg] \\
&-\frac{x}{H(m_{\phi_D})}\Bigg[\langle\Gamma\rangle_{\phi_D\to\chi N}\left(Y_{\phi_D} - Y_\chi\frac{Y^{eq}_{\phi_D}}{Y^{eq}_\chi}\right) + \theta(x-x_{ew})\langle\Gamma\rangle_{\phi_D\to\chi\nu}\left(Y_{\phi_D} - Y_\chi\frac{Y^{eq}_{\phi_D}}{Y^{eq}_\chi}\right)\Bigg],
\end{aligned} \tag{3.1}$$

$$\begin{aligned}
\frac{dY_\chi}{dx} = &\frac{1}{x^2}\frac{s(m_{\phi_D})}{H(m_{\phi_D})}\Bigg[\sum_{i=1}^{2}\langle\sigma v\rangle_{LH_i\to\phi_D\chi}(Y^{eq}_{\phi_D}Y^{eq}_\chi - Y_{\phi_D}Y_\chi) \\
&+\langle\sigma v\rangle_{W^\pm l^\mp\to\phi_D\chi}(Y^{eq}_{\phi_D}Y^{eq}_\chi - Y_{\phi_D}Y_\chi) + \langle\sigma v\rangle_{Z\nu\to\phi_D\chi}(Y^{eq}_{\phi_D}Y^{eq}_\chi - Y_{\phi_D}Y_\chi) \\
&+\langle\sigma v\rangle_{\phi_D^\dagger\phi_D\to\chi\chi}\left(Y^2_{\phi_D} - {Y_\chi}^2\frac{{Y^{eq}_{\phi_D}}^2}{Y^{eq2}_\chi}\right) + \langle\sigma v\rangle_{NN\to\chi\chi}\left(Y^{eq2}_N - {Y_\chi}^2\frac{Y^{eq2}_N}{Y^{eq2}_\chi}\right)\Bigg] \\
&+\frac{x}{H(m_{\phi_D})}\Bigg[\langle\Gamma\rangle_{\phi_D\to\chi N}\left(Y_{\phi_D} - Y_NY_\chi\frac{Y^{eq}_{\phi_D}}{Y^{eq}_NY^{eq}_\chi}\right) + \theta(x-x_{ew})\langle\Gamma\rangle_{\phi_D\to\chi\nu}\left(Y_{\phi_D} - Y_\chi\frac{Y^{eq}_{\phi_D}}{Y^{eq}_\chi}\right)\Bigg].
\end{aligned} \tag{3.2}$$

JHEP05(2022)182

The entropy density and Hubble parameter in terms of m_{ϕ_D} are

$$s(m_{\phi_D}) = \frac{2\pi^2}{45} g_*^s m_{\phi_D}^3, \quad H(m_{\phi_D}) = \frac{\pi}{\sqrt{90}} \frac{\sqrt{g_*}}{M_{pl}^r} m_{\phi_D}^3, \tag{3.3}$$

where $M_{pl}^r = 2.44 \times 10^{18}$ is the reduced Plank Mass. g_* and g_*^s are the effective degree of freedom related to the energy and entropy density of the universe, respectively at temperature $T = \frac{m_{\phi_D}}{x}$. Y_i^{eq} is the equilibrium number density of species i in comoving volume and is given by,

$$Y_i^{eq} = \frac{n_i^{eq}}{s} = \frac{45}{4\pi^4} \frac{g_i}{g_*^s} \left(\frac{m_i}{m_{\phi_D}} x \right)^2 K_2 \left(\frac{m_i}{m_{\phi_D}} x \right), \tag{3.4}$$

with m_i and g_i are the mass and the internal degree of freedom for particle i, and K_2 the order-2 modified Bessel function of the second kind. The thermal average width $\langle \Gamma_i \rangle$ of the species i is given by,

$$\langle \Gamma_{i \to jk} \rangle = \Gamma_{i \to jk} \frac{K_1\left(\frac{m_i}{m_{\phi_D}} x \right)}{K_2\left(\frac{m_i}{m_{\phi_D}} x \right)}. \tag{3.5}$$

The thermal average cross-section is given by [39],

$$\begin{aligned} \langle \sigma_{ij \to kl} v \rangle = & \frac{x}{128\pi^2 m_{\phi_D}} \frac{1}{m_i^2 m_j^2 K_2\left(\frac{m_i}{m_{\phi_D}} x \right) K_2\left(\frac{m_j}{m_{\phi_D}} x \right)} \\ & \times \int_{\left(m_i + m_j\right)^2}^{\infty} ds \frac{p_{ij} p_{kl} K_1\left(\frac{\sqrt{s}}{m_{\phi_D}} x \right)}{\sqrt{s}} \int |\bar{M}|^2 d\Omega, \end{aligned} \tag{3.6}$$

where s is the centre of mass energy, and $p_{ij}(p_{kl})$ are initial(final) centre of mass momentum. Finally, the relic density of the DM state χ is given by,

$$\Omega_\chi h^2 = \Omega_\chi^{TFI} h^2 + \frac{m_\chi}{m_{\phi_D}} \Omega_{\phi_D}^{FO} h^2, \tag{3.7}$$

where $\Omega_\chi^{TFI} h^2$ is the relic density obtained from the thermal freeze-in mechanism and $\Omega_{\phi_D}^{FO} h^2$ is the abundance of ϕ_D at the decoupling epoch T_d. In the above, the second term represents the super-wimp contribution to the DM relic abundance, which occurs due to the late decay of ϕ_D. The analytical expression for $\Omega_\chi^{TFI} h^2$ for the production of DM χ through the decay of ϕ_D is given by,

$$\Omega_\chi^{TFI} h^2 \simeq \frac{1.09 \times 10^{27}}{g_*^s \sqrt{g_*}} m_\chi \frac{g_{\phi_D} \Gamma_{\phi_D \to \chi N}}{m_{\phi_D}^2} \tag{3.8}$$

where g_{ϕ_D} is the internal degree of freedom for ϕ_D. For the analysis, we consider the following mass spectra, $M_N = 50\,\text{GeV}$, $M_{Z_{BL}} = 7\,\text{TeV}$, $M_{H_2} = 500\,\text{GeV}$, $m_{\phi_D} = 100\,\text{GeV}$ (unless mentioned otherwise), and the gauge coupling $g_{BL} = 0.9$. The choice of $M_{Z_{BL}}$ and g_{BL} is consistent with the constraint from CMS and ATLAS searches [40, 41]. The right-hand side of eq. (3.1) takes into account all possible number changing processes of ϕ_D to B/SM states as well as its decay.

JHEP05(2022)182

- This is to note, the depletion rate of ϕ_D via Z_{BL} mediated annihilation processes, i.e., $\phi_D^\dagger \phi_D \to Z_{BL} \to NN, \bar{f}f, H_2H_2$ is suppressed due to large Z_{BL} mass. Such processes decoupled from the cosmic soup much earlier compared to the annihilation of ϕ_D through contact interactions and processes mediated via B/SM Higgs(H_1, H_2), i.e., $\phi_D^\dagger \phi_D \to H_1/H_2 \to NN, \bar{f}f, H_2H_2$, etc.

- The annihilation of ϕ_D through contact interactions and s-channel mediated process via B/SM Higgs keeps the ϕ_D in the thermal bath for a longer time. When the respective interaction rate becomes less than the universe's expansion rate, ϕ_D decouples from the thermal bath.

- The depletion rate of ϕ_D via processes that are dependent on the dark sector Yukawa coupling $Y_{D\chi}$, such as $\chi\phi_D \to NZ_{BL}, N\phi_D \to \chi Z_{BL}$, etc. are highly suppressed because of small coupling strength $Y_{D\chi}$ and negligible abundance of χ at an early epoch.

- The decay of ϕ_D through $\phi_D \to \chi\nu$ process happens because of the active and sterile neutrino mixing which takes place after electroweak symmetry breaking (EWSB). The Heaviside step function, $\theta(x - x_{ew})$ ensures that decrease in the number density of ϕ_D via $\phi_D \to \chi\nu$ happens only after EWSB.

In eq. (3.2), the right-hand side contains all relevant processes to study the evolution of χ. As discussed earlier, production of χ is dominated by the decay process, i.e., $\phi_D \to \chi N$ compared to the annihilation of the bath particles. Based on the primary production mechanism of χ, there are two different scenarios.

- *Scenario-I*: The DM is primarily produced via the thermal freeze-in mechanism. This corresponds to the case where ϕ_D stays in the thermal bath for a more extended period of time owing to more considerable coupling strength with the bath particles. This tends to reduce its number density significantly. Thus its late decay gives negligible contribution to χ number density. Therefore, the correct relic density of χ is mostly obtained from the thermal freeze-in mechanism. This is illustrated in the left panel of figure 3.

- *Scenario-II*: The DM χ is primarily produced from the decay of ϕ_D after a freeze out, referred to as super-wimp mechanism. In this scenario, the number density of χ increases gradually through the thermal freeze-in mechanism, and at a later epoch, its number density increases significantly from the late decay of ϕ_D. This is to note that this scenario is possible to realise if ϕ_D decouples much earlier from the thermal bath due to suppressed interaction which leads to a large ϕ_D abundance at the time of decoupling. ϕ_D later decays completely to χ, significantly increasing the DM number density. We illustrate this schematically in the right panel of figure 3.

Before focusing on the main study of this work, we want to bring attention to the readers that ϕ_D must decay before the big bang nucleosynthesis (BBN). The decay of ϕ_D adds relativistic species to the thermal bath, which may alter the standard BBN scenario, and hence will be severely constrained. To avoid such conflict, we demand that lifetime

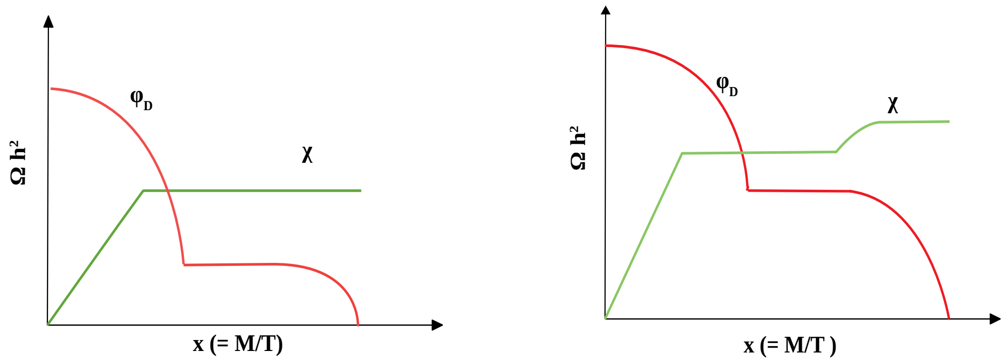

Figure 3. Left panel: schematic diagram representing freeze-in dominated scenario. Right panel: schematic diagram representing super-wimp dominated scenario.

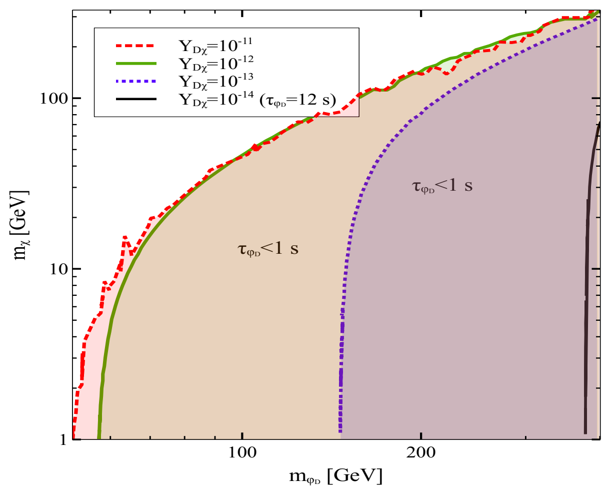

Figure 4. Lifetime contours of ϕ_D in m_χ and m_{ϕ_D} plane for fixed values of the coupling $Y_{D\chi}$. For each of the chosen $Y_{D\chi}$, the shaded region is allowed from BBN, where lifetime of ϕ_D is less than 1 second.

of ϕ_D must be less than 1 sec which puts a lower bound on dark sector Yukawa coupling $Y_{D\chi}$, via which ϕ_D decays. In figure 4, we show the lifetime contour of the ϕ_D state for each of the given Yukawa coupling $Y_{D\chi}$, where we vary the mass m_χ of the DM and the mass of the parent particle m_{ϕ_D}. For each of the chosen $Y_{D\chi}$ values, the shaded region is allowed from BBN. We note that one of the products of the ϕ_D decay is N, where N further decays to the SM particles and adds relativistic species to the thermal bath. The decay length of RHN depends on the active-sterile neutrino mixing, which depends on the light neutrino masses and PMNS mixing angles. We provide the expressions for the decay width of ϕ_D and N in the appendix. For $M_N > m_{W^\pm}, m_Z$, N decays dominantly through 2 body processes, such as, $N \to l^\pm W^\mp$ and $N \to Z\nu$. For $M_N < m_{W^\pm}, m_Z$ which we

JHEP05(2022)182

consider in this study, RHN decays to the three SM fermions through off-shell W, and Z gauge bosons. For our choice of mass parameter M_N, we have checked that the decay of N to SM states takes place instantaneously and is not constrained from BBN.

One can additionally set a upper bound on dark sector Yukawa coupling $Y_{D\chi}$ by demanding that ϕ_D decays to χ after ϕ_D freezes-out (at $T \sim m_{\phi_D}/25$). This requirement implies,

$$\Gamma_{\phi_D \to \chi N} \leq H(m_{\phi_D}) \xRightarrow{m_{\phi_D}=100\,\text{GeV}} Y_{D\chi} \leq 10^{-8} \tag{3.9}$$

In this work we consider such values of $Y_{D\chi}$, so that both the BBN and the above mentioned constrained are satisfied. The entropy of the universe increases after the decay of ϕ_D. The increase in entropy can be approximated [42] as,

$$\frac{\Delta s}{s} \approx \frac{n_{\phi_D}(m_{\phi_D} - m_\chi)}{sT} \approx \frac{Y_{\phi_D}(m_{\phi_D} - m_\chi)}{T} \tag{3.10}$$

Due to the small value of $Y_{D\chi}$, ϕ_D decays in the late epoch of the universe when the universe temperature is around MeV. This leads to negligible amount of increase in entropy density in the universe, otherwise such increase in entropy can dilute the DM produced in an early epoch.

3.2 ϕ_D abundance

Since a significantly large number of χ is produced from the late decay of ϕ_D; therefore the abundance of ϕ_D at the time of decoupling plays a vital role in determining the correct DM relic density. A large abundance of ϕ_D will contribute significantly in the χ production via $\phi_D \to \chi N$ late decay. As discussed before, ϕ_D was in equilibrium with the SM particles because of the large scalar quartic couplings $\lambda_{SD}, \lambda_{Dh}$ and SM-BSM Higgs mixing angle $\sin\theta$. The most dominant annihilation channels for ϕ_D, $\phi_D^\dagger \phi_D \to W^+W^-, ZZ, NN$ mediated via SM-like Higgs state H_1, for which we provide the analytic expressions of the cross-section in the appendix, and show the variation of thermal average cross-section $\langle\sigma v\rangle_{FO}$ at T_d in figure 6(b). The H_2 mediated contribution is relatively smaller due to heavy propagator suppression, except the region of the H_2 resonance. In figure 5, we show the scatter plots in the λ_{SD} and λ_{Dh} plane for the three different values of mixing angle $\sin\theta$, for which $\Omega_{\phi_D}^{FO}h^2$ varies in between a) $0.01 < \Omega_{\phi_D}^{FO}h^2 < 0.12$ (for the top left panel plot), b) $0.12 < \Omega_{\phi_D}^{FO}h^2 < 1$ (for the top right panel plot), and c) $1.0 < \Omega_{\phi_D}^{FO}h^2 < 10.0$ (for the bottom plot). The ϕ_D abundance at T_d is mostly governed by the couplings λ_{SD}, λ_{Dh} and $\sin\theta$. Comparing the horizontal and vertical bands between different panels, for a fixed value of $\sin\theta$, decreasing λ_{SD} and λ_{Dh} will lead to a higher $\Omega_{\phi_D}^{FO}h^2$. This typically occurs, as with the decrease in the relevant quartic coupling, the interaction rate of ϕ_D decreases, resulting in an early freeze-out of ϕ_D, which subsequently gives a larger ϕ_D abundance. On the other hand, in each of these three panels, for a fixed value of λ_{Dh}, as we decrease $\sin\theta$ from 0.1 to 0.01 and further, a larger λ_{SD} coupling is required to compensate the decrease in the interaction strength and to maintain $\Omega_{\phi_D}^{FO}h^2$ in the given range. The cone-shaped region in each of the plots represents a cancellation in the $\phi_D^\dagger \phi_D H_1$ vertex that we will discuss later. Due to a

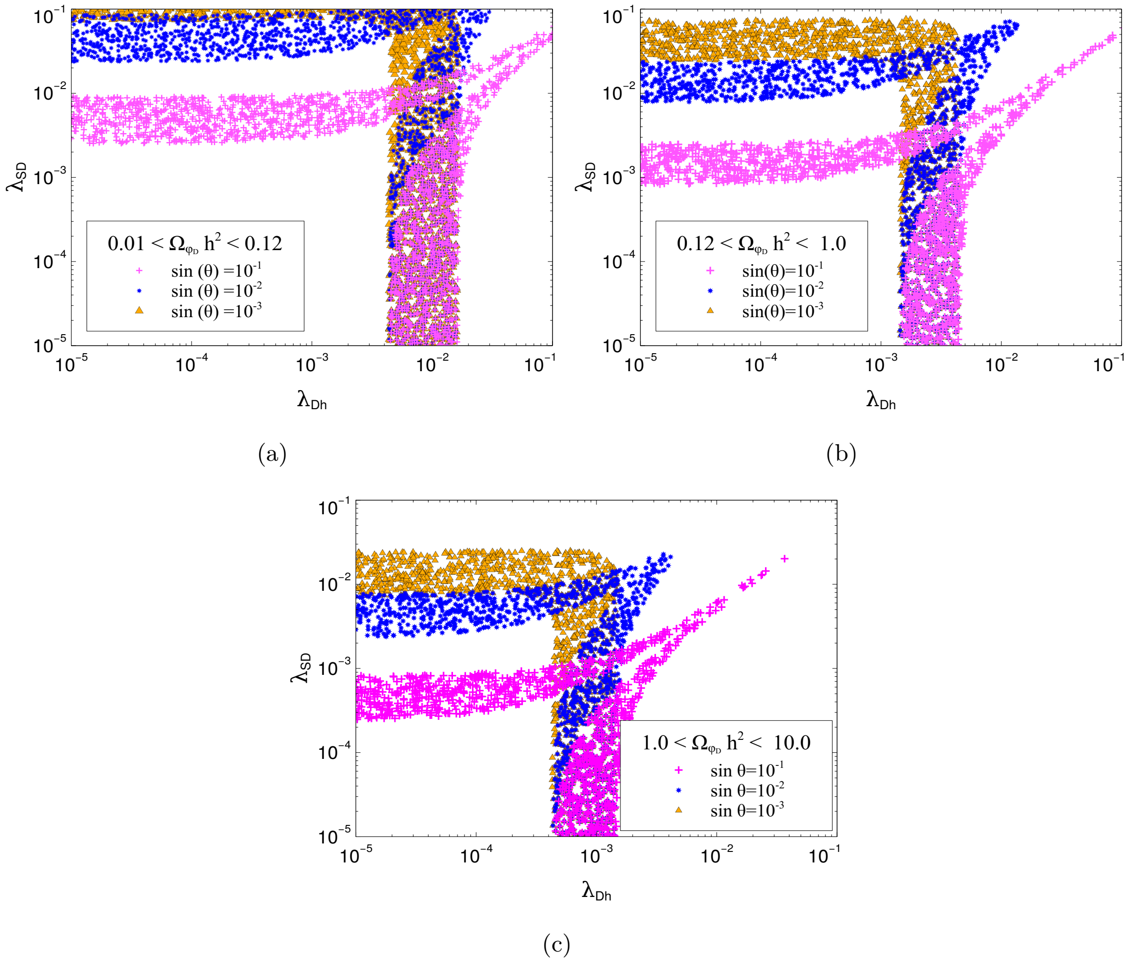

Figure 5. We show the scatter plot in λ_{Dh}-λ_{SD} plane for the different values of $\sin\theta$ and demanding $\Omega^{FO}_{\phi_D}h^2$ in the range 0.01 to 0.12 in figure 5(a). Similarly, demanding $\Omega^{FO}_{\phi_D}h^2$ in the range 0.12 to 1.0 shown in figure 5(b) and for $\Omega^{FO}_{\phi_D}h^2$ greater than 1.0 shown in figure 5(c).

relative suppression in the vertex factor, the interaction rate decreases, thereby leading to a higher value of $\Omega^{FO}_{\phi_D}h^2$. To maintain $\Omega^{FO}_{\phi_D}h^2$ in the given range, hence a larger value of couplings λ_{SD} and λ_{Dh}, and a large thermal averaged cross-section $\langle\sigma v\rangle$ are required. To further explore the effect of an early and late decoupling of ϕ_D on DM number density, we consider two benchmark points which are as follows,

1. $\lambda_{SD} = 10^{-1}$, $\sin\theta = 0.3$, $\lambda_{Dh} = 10^{-5}$.

2. $\lambda_{SD} = 10^{-2}$, $\sin\theta = 10^{-2}$, $\lambda_{Dh} = 4\times 10^{-3}$.

In figure 6(a), we show the variation of ϕ_D abundance at T_d with the change in ϕ_D mass for these two above mentioned benchmark points. The red line in figure 6(a) corresponds to our first benchmark point, where ϕ_D stays in thermal equilibrium for a longer period due to a large interaction rate with the bath particles which happen because of a large $\sin\theta$ and λ_{SD}. In figure 6(b), we show the variation of thermal average cross-section $\langle\sigma v\rangle_{FO}$ at T_d

JHEP05(2022)182

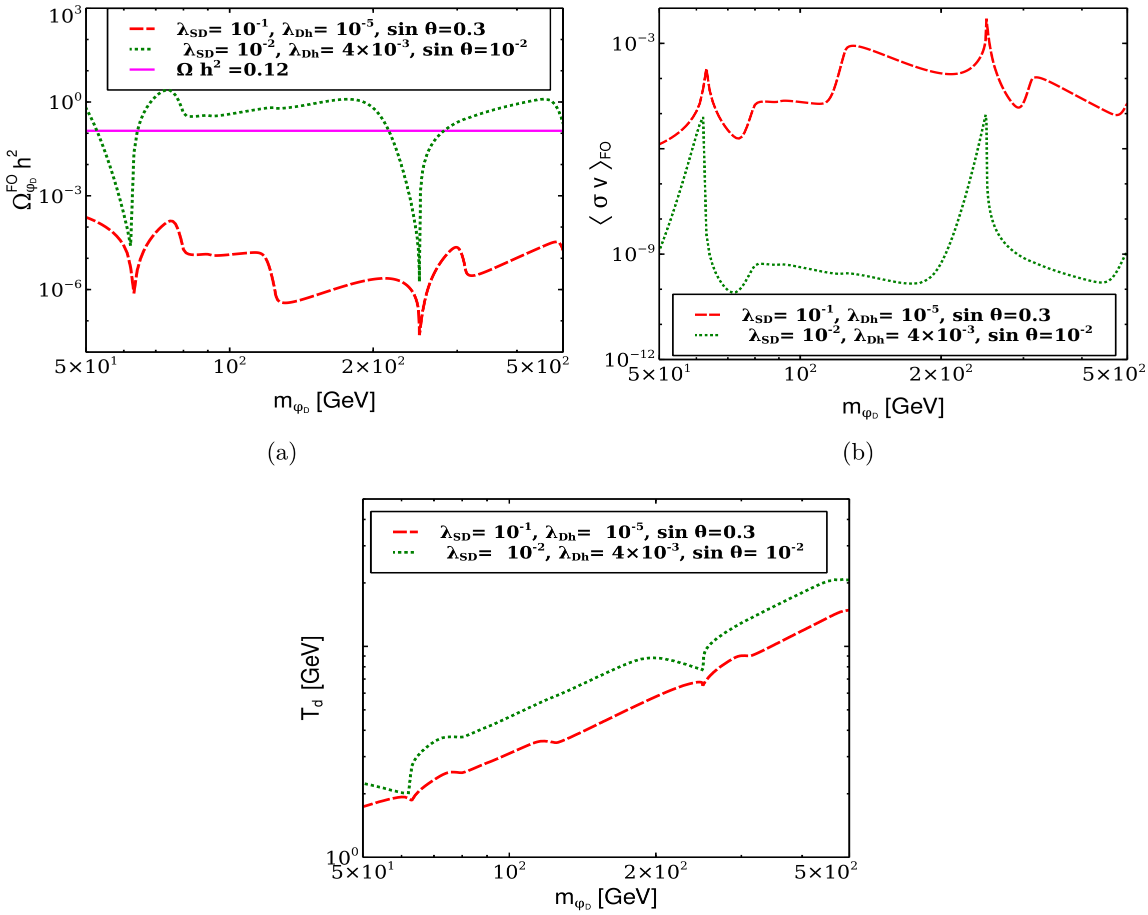

(a) (b) (c)

Figure 6. Figure 6(a), and figure 6(b) represent the variation of $\Omega^{FO}_{\phi_D}h^2$, and $\langle\sigma v\rangle_{FO}$ with mass of ϕ_D, and figure 6(c) represent the variation of the freeze-out temperature of ϕ_D w.r.t. its mass.

with the mass of ϕ_D. As we can see there are few sudden increases in $\langle\sigma v\rangle_{FO}$ w.r.t. m_{ϕ_D}. When the mass of ϕ_D becomes half of the mass of SM-like Higgs H_1, s channel resonance mediated via H_1 takes place, and $\langle\sigma v\rangle_{FO}$ increases significantly. After which, it decreases with the increase in mass of ϕ_D. For $m_{\phi_D} \approx 80.4\,\text{GeV}$, thermal average cross-section $\langle\sigma v\rangle_{FO}$ further increases. This occurs as the channel $\phi_D^\dagger\phi_D \to W^+W^-$ opens up. Similar increase in $\langle\sigma v\rangle_{FO}$ occurs when $m_{\phi_D} \approx m_{H_1}$, it is when $\phi_D^\dagger\phi_D \to H_1H_1$ opens up. Thereafter $\langle\sigma v\rangle_{FO}$ decreases with the increase in mass of ϕ_D except around $m_{\phi_D} \approx 250\,\text{GeV}$. It is where s channel resonance mediated via H_2 occurs which enhances $\langle\sigma v\rangle_{FO}$ significantly. For thermal dark sector particle ϕ_D, the abundance $\Omega^{FO}_{\phi_D}h^2$ is inversely proportional to $\langle\sigma v\rangle_{FO}$, which is evident from the figure. In each of these three panels, the green line corresponds to the second benchmark point, for which interaction of ϕ_D is suppressed owing to a smaller coupling λ_{SD} and mixing angle $\sin\theta$. The variation of $\Omega^{FO}_{\phi_D}h^2$ and $\langle\sigma v\rangle_{FO}$ with the change in ϕ_D mass is similar to the first benchmark point. It is important to note that due to suppressed interaction, ϕ_D decouples from the thermal bath much earlier, leading to a large

JHEP05(2022)182

Vertex	Vertex Factor
$\phi_D^\dagger\,\phi_D\,Z_{BL\mu}$	$\lambda_{Z_{BL}} = g_{BL}(p_2 - p_1)^\mu$
$\phi_D^\dagger\,\phi_D\,H_1$	$\lambda_{H_1} = (\lambda_{Dh} v\cos\theta - \lambda_{SD} v_{BL}\sin\theta)$
$\phi_D^\dagger\,\phi_D\,H_2$	$\lambda_{H_2} = -(\lambda_{Dh} v\sin\theta + \lambda_{SD} v_{BL}\cos\theta)$

Table 2. Couplings of ϕ_D with Z_{BL}, H_1 and H_2.

Vertex	Vertex Factor
$H_1VV(V = W, Z)$	$2m_V^2\cos\theta/v$
$H_2VV(V = W, Z)$	$2m_V^2\sin\theta/v$
$H_1ff(f = t, b)$	$2m_f\cos\theta/v$
$H_2ff(f = t, b)$	$2m_f\sin\theta/v$
H_1NN	$y_N\sin\theta/\sqrt{2}$
H_2NN	$y_N\cos\theta/\sqrt{2}$

Table 3. Couplings of SM and BSM Higgs with SM fermions, RHN and gauge bosons.

relic density of ϕ_D. This is also reflected in figure 6(c), which shows the variation of the freeze-out temperature of ϕ_D with its mass for these two benchmark points. As it is evident, the freeze-out temperature is relatively smaller for the first benchmark point, and hence freeze-out of ϕ_D occurs at a later epoch. The sudden dip in the freeze-out temperature around $\phi_D \sim 60$ GeV and 250 GeV occur because of s-channel resonance mediated via H_1 and H_2. As the $\langle\sigma v\rangle_{FO}$ increases significantly in this region, this enables ϕ_D to remain in a thermal bath for a long time. The first benchmark point corresponds to *Scenario-I*, and the second benchmark point corresponds to *Scenario-II*, discussed earlier.

In figure 7(a), 7(b) and 7(c), we show the variation of ϕ_D abundance at T_d with the parameters λ_{SD}, λ_{Dh} and $\sin\theta$. We re-emphasize, the dominant annihilation mode for ϕ_D are $\phi_D^\dagger\phi_D \to W^+W^-, ZZ, NN$ which are mediated via H_1 and H_2.[2] The other process, such as $\phi_D^\dagger\phi_D \to \bar{f}f$ contribute negligibly in ϕ_D annihilation, as they are suppressed by the small mass of the final state fermions. In figure 7(a), we show the variation of $\Omega_{\phi_D}^{FO}h^2$ with λ_{Dh} while keeping λ_{SD} and $\sin\theta$ fixed to few sets of values. As we can see from the green line which corresponds to $\lambda_{SD} = 10^{-3}$ and $\sin\theta = 10^{-1}$, $\Omega_{\phi_D}^{FO}h^2$ remains independent of λ_{Dh} in between 10^{-5} to 10^{-4}. This occurs as the effective vertex factor involving $\phi_D^\dagger\phi_D H_1$ for such a small value of λ_{Dh} is governed by λ_{SD} and $\sin\theta$ rather than λ_{Dh}. This can be understood from the expression of the vertex factors, which we provide in table 2. We also provide the vertex factors of different $H_{1,2}$ interactions with the SM fermions and gauge bosons in table 3. In between $10^{-5} < \lambda_{Dh} < 10^{-4}$, dominant annihilation modes are $\phi_D^\dagger\phi_D \to W^+W^-, ZZ$ mediated by SM Higgs boson H_1. As λ_{Dh} increases, effective vertex

[2]For $\phi_D^\dagger\phi_D \to W^+W^-, ZZ$, H_2 mediated process is suppressed due to small $\sin\theta$ and heavy mass of H_2. However, for $\phi_D^\dagger\phi_D \to NN$, H_1 mediated process is suppressed due to $\sin\theta$.

JHEP05(2022)182

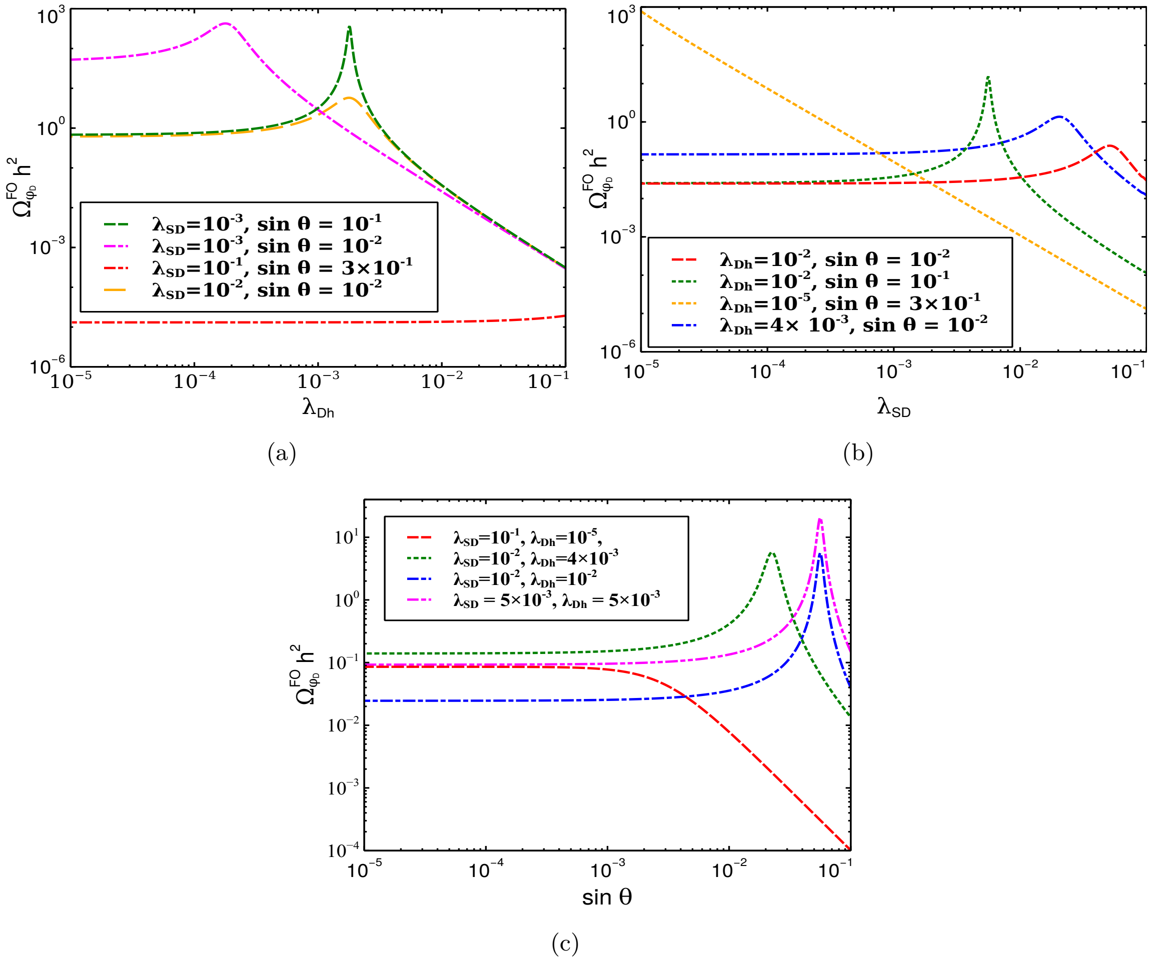

Figure 7. Figure 7(a) and figure 7(b) show the variation of the relic abundance of ϕ_D with the couplings λ_{DH} and λ_{SD}, respectively. Figure 7(c) shows the variation of relic abundance of ϕ_D with $\sin\theta$.

factor involving $\phi_D\phi_D^\dagger H_1$ decreases due to a relative cancellation between different terms in the respective expression (see table 2), leading to a suppressed annihilation rate. This results in an increase in the $\Omega^{FO}_{\phi_D}h^2$ as λ_{Dh} increases from $\lambda_{Dh}\approx 10^{-4}$ to $\lambda_{Dh}\approx 2\times10^{-3}$. This is to note that in this region annihilation rate $\phi_D^\dagger\phi_D \to NN$ contributes more than $\phi_D^\dagger\phi_D \to W^+W^-, ZZ$. This occurs as the process $\phi_D^\dagger\phi_D \to NN$ mediated by H_2 dominates as λ_{H_2} becomes larger than λ_{H_1} and also the process is not suppressed by scalar mixing angle. As λ_{Dh} further increases, λ_{H_1} increases which makes the annihilation rate of ϕ_D large. This results in a decrease in $\Omega^{FO}_{\phi_D}h^2$ as λ_{Dh} in between $2\times10^{-3} < \lambda_{Dh} < 10^{-1}$. The magenta and the yellow line follow the same characteristics as the green line. The difference in the abundance of ϕ_D for different lines arises due to different choices of λ_{SD} and $\sin\theta$. For a very large λ_{Dh}, the green, yellow and magenta lines merge as λ_{H_1} is governed by the λ_{Dh} only. The red line corresponds to a much larger value of $\lambda_{SD}=10^{-1}$ and $\sin\theta = 0.3$. For this chosen parameter, λ_{H_1} is governed by λ_{SD} only. This makes the relic abundance of ϕ_D at T_d independent of λ_{Dh}.

In figure 7(b), we show the variation of $\Omega_{\phi_D}^{FO}h^2$ w.r.t. the coupling λ_{SD}. For the chosen parameters corresponding to the red, green and blue lines, $\Omega_{\phi_D}^{FO}h^2$ is independent of λ_{SD} for minimal coupling. In this scenario, λ_{H_1} is governed by λ_{Dh} only. As for both the green and red lines, the chosen value of λ_{Dh} is the same and $\cos\theta \approx 1$, therefore both of these lines give similar contributions to the $\Omega_{\phi_D}^{FO}h^2$ for small λ_{SD}. The blue line corresponds to a relatively smaller value of λ_{Dh} compared to the green and red line, because of which $\Omega_{\phi_D}^{FO}h^2$ is larger for blue line due to low interaction rate, in the region where λ_{SD} is very small. As λ_{SD} increases, the second term in the λ_{H_1} becomes larger. This leads to cancellation in the respective vertex due to a difference in the sign between the first and second terms. Similar to figure 7(a), the suppression in the effective vertex leads to an increase in $\Omega_{\phi_D}^{FO}h^2$. In the cancellation region, the most dominant annihilation channel is $\phi_D^\dagger\phi_D \to NN$. For the yellow line, λ_{Dh} is considered to be negligible because of which λ_{H_1} is governed by its second term only. Thus, as λ_{SD} increases, the annihilation rate of ϕ_D also increases which result in a decrease in $\Omega_{\phi_D}^{FO}h^2$. In figure 7(c), we show the variation of $\Omega_{\phi_D}^{FO}h^2$ w.r.t. $\sin\theta$. Similar to figure 7(a) and figure 7(b), for very small $\sin\theta$, few of the lines represent similar values of ϕ_D abundance, as the interaction rate is totally governed by $\lambda_{Dh}\cos\theta$ combination in the λ_{H_1}. The cancellation in λ_{H_1} takes place only at a larger value of $\sin\theta$, for which $\Omega_{\phi_D}^{FO}h^2$ increases significantly. For the chosen parameter corresponding to the red line, λ_{SD} is much larger than λ_{Dh}. Therefore, in this region, the annihilation rate is governed by the second term of λ_{H_1}, because of which $\Omega_{\phi_D}^{FO}h^2$ decreases for larger values of $\sin\theta$ due to an increase in the annihilation rate.

3.3 ϕ_D and χ abundance in *Scenario-I* and *Scenario-II*

Figure 8 corresponds to *Scenario-I*, for which primary contribution to the DM relic density arises from thermal freeze-in production of χ. For the evaluation of $\Omega_{\phi_D}^{FO}h^2$ and $\Omega_\chi h^2$, we consider benchmark point 1. This is evident from figure 8(a) that ϕ_D stays in the thermal bath for a significantly longer time owing to a large λ_{SD} and $\sin\theta$. Due to this, the abundance of ϕ_D is reduced significantly before it freezes out, and therefore, its contribution to the production of χ via late decay is negligible. For this figure, we consider a $Y_{D\chi}$ which is in agreement with the BBN constraint as well as eq. (3.9). The lifetime of ϕ_D increases with the increase in χ mass, thereby leading to the differences that can be seen from yellow, blue, green and red lines in the plot.

In figure 8(b), we show the thermal freeze-in production of χ, production of χ from the out of equilibrium decay of ϕ_D, and the relic abundance of χ including both the contributions. At a very early epoch, the abundance of χ was vanishingly small due to suppressed interaction of χ with bath particles owing to small coupling strength $Y_{D\chi} \sim 10^{-12}$. For our chosen parameters, the production of χ is, however, primarily governed by the decay of ϕ_D to χN state. The thermal freeze-in production of χ ceases as soon as the temperature of the thermal bath becomes less than the mass of ϕ_D. In evaluating the relic abundance of χ, we have neglected the inverse decay process $\chi N \to \phi_D$, as due to a very small abundance of χ, inverse decay is entirely negligible. Due to this, the freeze-in temperature of χ in our analysis is independent of abundance of χ but rather depends on m_{ϕ_D}. The abundance of χ can further be enhanced through the out of equilibrium decay

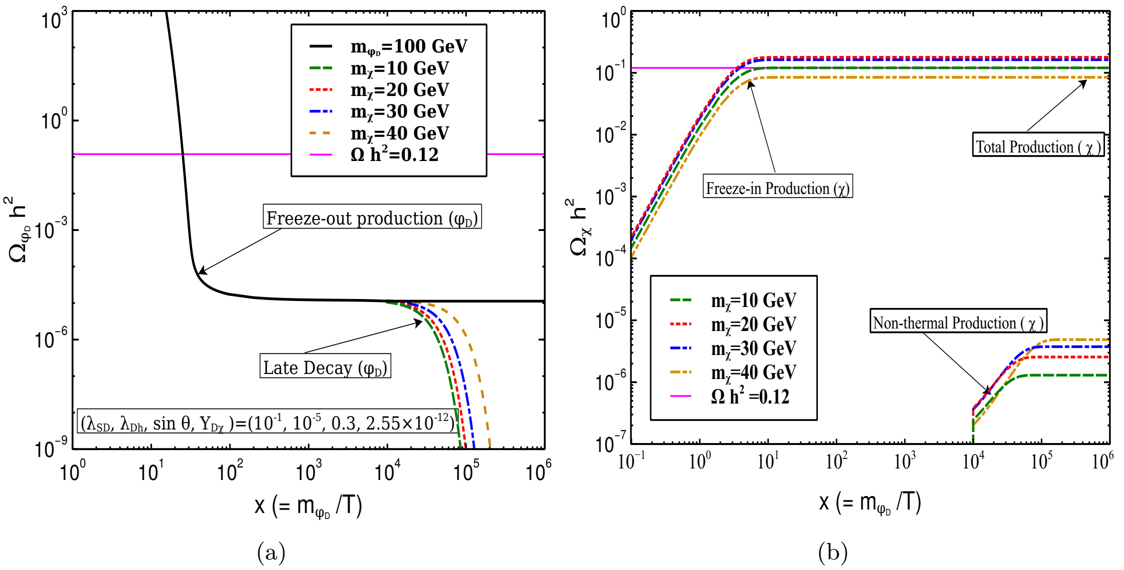

Figure 8. Left panel: figure 8(a) shows the variation of $\Omega_{\phi_D} h^2$ w.r.t. x. Right panel: figure 8(b) shows the variation of $\Omega_\chi h^2$ w.r.t. x. This corresponds to the freeze-in dominated scenario.

of ϕ_D. However, in this scenario, non-thermal production of χ from the late decay of ϕ_D is tiny, as has been shown in figure 8. Therefore, the total production of χ, in this case, is determined by the thermal freeze-in mechanism. It is also important to highlight that the production of χ through the late decay of ϕ_D increases as the mass of χ increases, as can be understood from eq. (3.7). And it is also evident from the lower right side of figure 8(b), where we show the non-thermal contribution to relic abundance of $\Omega_\chi h^2$ for different χ masses.

Contrary to the previous scenario *Scenario-I*, figure 9 captures all the details about *Scenario-II*, where late decay of ϕ_D contributes significantly in the production of χ. As it is evident from figure 9(a) that ϕ_D decouples from the thermal bath much earlier due to suppressed interaction with the bath particles. The abundance of ϕ_D at T_d is therefore much larger than the ϕ_D abundance for *Scenario-I*, and its out-of-equilibrium decay can contribute significantly to the χ abundance. This has been shown in figure 9(b), where we show the evolution of χ abundance. At high temperatures, the thermal freeze-in mechanism governs the production of χ. Similar to the previous scenario, at this very early epoch, the dominant freeze-in production mode of χ is from ϕ_D decay. It is important to highlight that as the mass of χ increases from $m_\chi = 50\,\text{GeV}$ to $m_\chi = 75\,\text{GeV}$, the thermal freeze-in contribution decreases instead of increase. It is due to the fact that phase space suppression for $\phi_D \to \chi N$ increases as mass of χ increases from $m_\chi = 50\,\text{GeV}$ to $m_\chi = 75\,\text{GeV}$. At a later epoch, out of equilibrium decay of ϕ_D starts to contribute to the production of χ. As one can see, the out of equilibrium decay of ϕ_D alone can overproduce the χ. For our choice of parameters, the DM relic abundance is satisfied if $m_\chi = 6.5\,\text{GeV}$.

In figure 10, we show the effect of dark sector coupling $Y_{D\chi}$ on the production of ϕ_D and χ. As one sees from figure 10(a) that change in $Y_{D\chi}$ only changes the lifetime of ϕ_D.

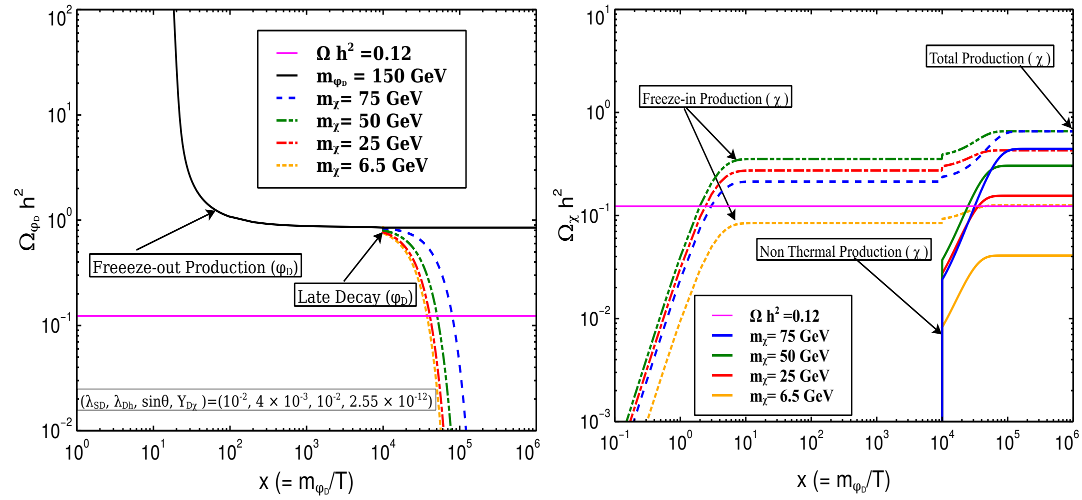

(a) (b)

Figure 9. Left panel: figure 9(a) shows the variation of $\Omega_{\phi_D}h^2$ w.r.t. x. Right panel: figure 9(b) shows the variation of $\Omega_\chi h^2$ w.r.t. x. This corresponds to the super-wimp dominated scenario.

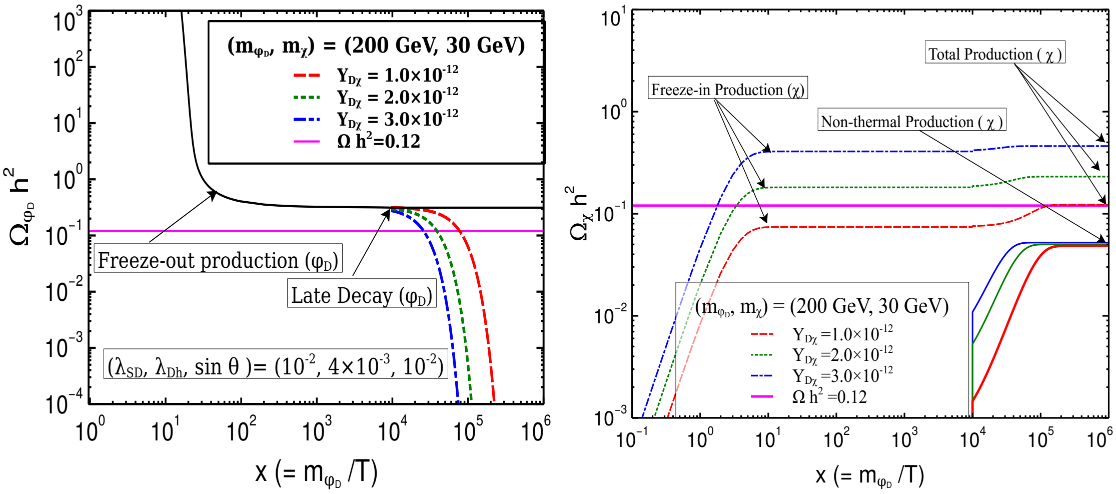

(a) (b)

Figure 10. Left panel: figure 10(a) shows the variation of $\Omega_{\phi_D}h^2$ w.r.t. x. Right panel: figure 10(b) shows the variation of $\Omega_\chi h^2$ w.r.t. x. This corresponds to a mixed scenario, where both the freeze-in and super-wimp contributions are significant.

Owing to a small value of $Y_{D\chi}$, it does not have any effect in the freeze-out processes of ϕ_D. In figure 10(b), we show that the thermal freeze-in production of χ increases as $Y_{D\chi}$ increases. Since ϕ_D abundance is independent of $Y_{D\chi}$ coupling, hence, production of χ from late decay of ϕ_D is also independent of dark sector coupling $Y_{D\chi}$. For the parameter choice, both the thermal freeze-in and non-thermal contributions are significant in the production of DM χ. Figure 11 shows the variation of $\Omega^{FO}_{\phi_D}h^2$ w.r.t. x for different choices of m_{ϕ_D}. As one can see from the left panel (figure 11(a)) that ϕ_D yield increases as we

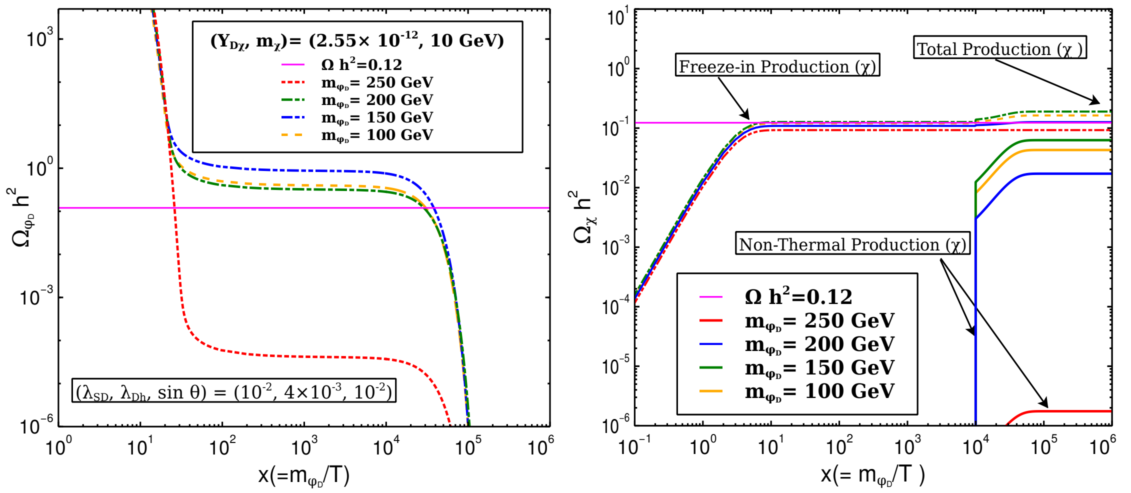

(a) (b)

Figure 11. Left panel: figure 11(a) shows the variation of $\Omega_{\phi_D} h^2$ w.r.t. m_{ϕ_D}. Right panel: figure 11(b) shows the variation of $\Omega_\chi h^2$ w.r.t. x.

vary $m_{\phi_D} = 100\,\text{GeV}$ to $m_{\phi_D} = 150\,\text{GeV}$. However, for even larger m_{ϕ_D} values, such as, 200 and 250 GeV, the $\Omega^{FO}_{\phi_D} h^2$ decreases as annihilation processes of ϕ_D approaches s-channel resonances mediated via H_2. This in turn effects the production of χ from the late decay of ϕ_D. As one can see from figure 11(b), the thermal freeze-in production of χ at high temperature increases as the mass of ϕ_D decreases. This occurs because $T_{FI} \sim m_{\phi_D}$, and a lower T_{FI} leads to higher production. At a later epoch, non-thermal production of χ from the late decay of ϕ_D starts to contribute. The non-thermal production of χ increases as mass of ϕ_D increases from 100 to 150 GeV, but later decreases with the increase in the mass of ϕ_D.

3.4 Dependence of $Y_{D\chi}$ on model parameters

In figure 12, we show the dependence of dark sector Yukawa coupling $Y_{D\chi}$ which governs the abundance of χ via thermal freeze-in production on parameters which determine the abundance of ϕ_D at the time of decoupling. In figure 12(a), we show dependence of $Y_{D\chi}$ on m_{ϕ_D} for our two scenarios.

- The thermal freeze-in dominated scenario, i.e., *Scenario-I* is represented by the red and green lines in the figure. In this scenario, ϕ_D has a negligible abundance after freeze-out from the thermal bath, which is evident from the red line of figure 6(a). To show the dependence of $Y_{D\chi}$ on m_{ϕ_D}, we have considered two different masses of χ which are 10 and 20 GeV. The thermal freeze-in production ceases when the temperature of the thermal bath becomes less than m_{ϕ_D}. The freeze-in temperature drops as we consider a lighter ϕ_D state. For the lower mass of ϕ_D, production of χ, therefore, takes place for a longer time which in turn increase the abundance of χ significantly. To satisfy the correct relic density, we can decrease the production of χ by decreasing the dark sector Yukawa coupling $Y_{D\chi}$. This behaviour is opposite

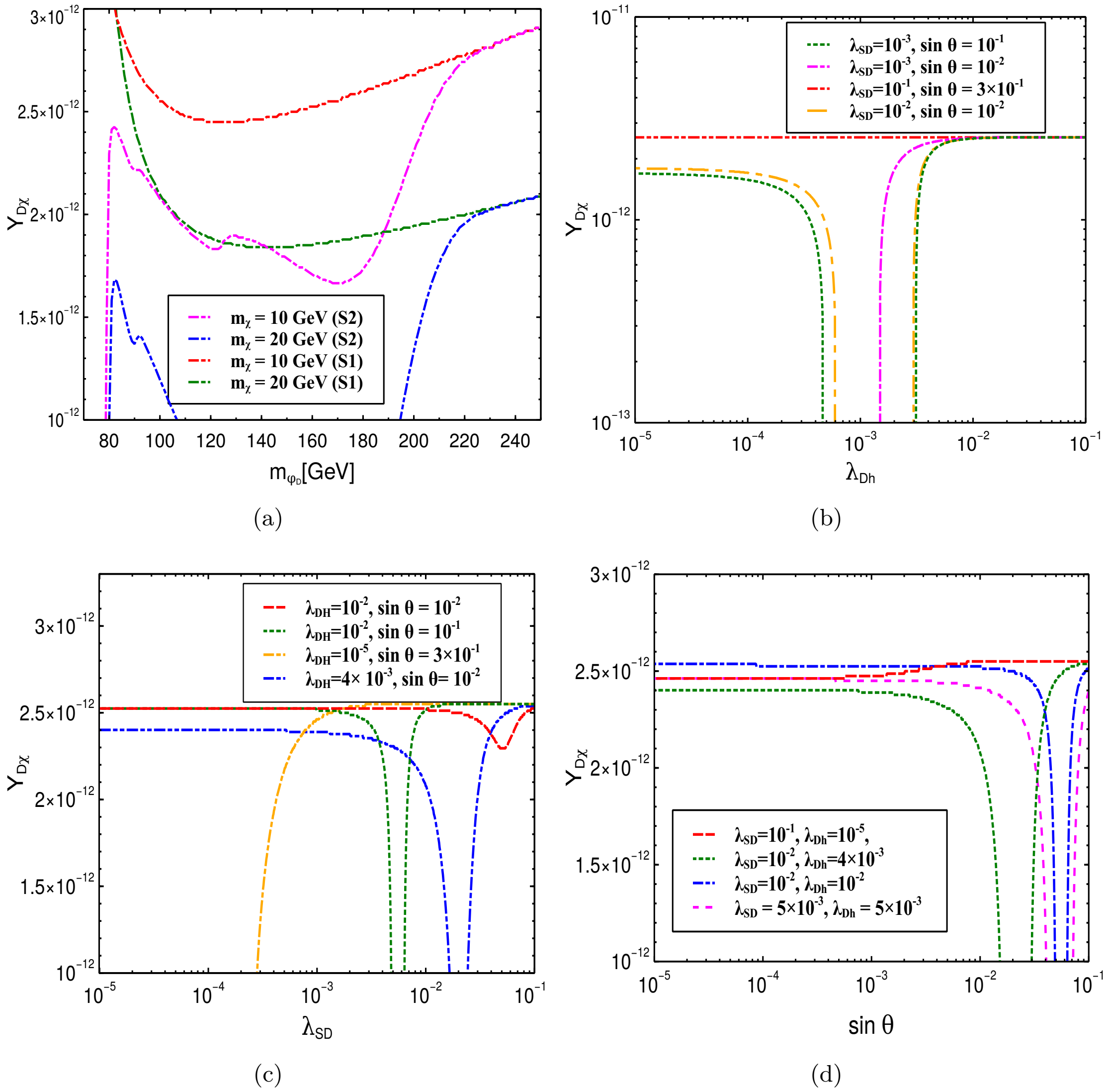

Figure 12. Figure 12(a) shows the contour of $\Omega h_\chi^2 = 0.12$ in the coupling $Y_{D\chi}$ and mass of ϕ_D (m_{ϕ_D}) plane. Figure 12(b) shows the same in $Y_{D\chi}$ and λ_{Dh} plane, figure 12(c) and figure 12(d) show the same in the $Y_{D\chi}$-λ_{SD}, and $Y_{D\chi}$- $\sin\theta$ plane. The parameter chosen for this plot are as follows, $m_S = 500\,\text{GeV}$, $M_N = 50\,\text{GeV}$, $m_\chi = 10\,\text{GeV}$, $m_{\phi_D} = 100\,\text{GeV}$, $g_{BL} = 0.9$, $m_{Z_{BL}} = 7\,\text{TeV}$.

for a large mass of ϕ_D. The freeze-in production of χ suffers Boltzmann suppression at a much higher temperature compared to the case of the low mass of ϕ_D. To compensate this effect, the production rate needs to be increased, which is done by increasing the magnitude of $Y_{D\chi}$. It is important to highlight that as mass of ϕ_D decreases from $m_{\phi_D} = 120\,\text{GeV}$ to $m_{\phi_D} = 80\,\text{GeV}$, the magnitude of $Y_{D\chi}$ increases instead of decrease. It is due to fact that the phase space suppression for $\phi_D \to \chi N$ process increases as mass of ϕ_D decreases from $m_{\phi_D} = 120$ GeV to $m_{\phi_D} = 80\,\text{GeV}$. The behaviour of these two curves, even though similar, however the required value of $Y_{D\chi}$ is more prominent for the lower mass of χ compared to the higher mass of χ.

- The variation of the required $Y_{D\chi}$ for *Scenario-II* which satisfies the DM relic abundance is shown by the pink and blue lines in figure 12(a). $\Omega^{FO}_{\phi_D}h^2$ for *Scenario-II* is shown via the green coloured line in figure 6(a), which indicates $\Omega^{FO}_{\phi_D}h^2 \geq 0.12$ except the region near s-channel resonance around $m_{\phi_D} = M_{H_1}/2 \sim 62.5\,\text{GeV}$ and $m_{\phi_D} = M_{H_2}/2 \sim 250\,\text{GeV}$. The large abundance of ϕ_D enhances the relic density of χ. The late decay of ϕ_D producing χ is independent of the Yukawa coupling $Y_{D\chi}$; however, the thermal contribution depends on $Y_{D\chi}$. Hence, depending upon the abundance of ϕ_D, the dark sector Yukawa coupling $Y_{D\chi}$ needs to be tuned accordingly to satisfy the relic density constraint. It is important to highlight that the out-of-equilibrium decay of ϕ_D in the production of χ can be so significant that to satisfy the correct relic abundance of χ, the thermal freeze-in production of χ is required to be small, which is possible to achieve for a small $Y_{D\chi}$. However, note that the coupling $Y_{D\chi}$ can not be made arbitrarily small, as the BBN imposes a strong lower bound on $Y_{D\chi}$.

  The pink and blue lines in figure 12(a) along which the DM relic abundance $\Omega_\chi h^2 = 0.12$ show the variation of the required $Y_{D\chi}$ w.r.t. ϕ_D mass for this scenario. The pink line clearly shows that a smaller value of $Y_{D\chi}$ is required in order to satisfy the correct relic density for *Scenario-II* when compared to the red line, which corresponds to the thermal freeze-in dominated scenario of *Scenario-I*. Also, note that the pink and red lines merge for the mass of ϕ_D greater than 200 GeV. For $m_{\phi_D} \sim 250\,\text{GeV}$, due to the s-channel resonance, the abundance of ϕ_D decreases significantly (see figure 6(a)). Therefore, a large thermal freeze-in contribution is required to satisfy the correct relic abundance, which in turn demands a larger value of the Yukawa coupling $Y_{D\chi}$. The blue line traces the pink line in part of the parameter space, with the notable difference that the out of equilibrium decay of ϕ_D producing χ is more dominant in between 110–190 GeV. The relic abundance of χ in this region becomes larger than the observed relic density due to the large contribution from the late decay of ϕ_D. Hence, for no value of $Y_{D\chi}$, the DM relic density constraint $\Omega_\chi h^2 = 0.12$ is satisfied.

In figure 12(b), we show dependence of $Y_{D\chi}$ on λ_{Dh}. The observations are listed as follows:

- The red line in this figure represents *Scenario-I*, i.e., the thermal freeze-in dominated scenario. In figure 7(a), the red line shows the variation of $\Omega^{FO}_{\phi_D}h^2$ with λ_{Dh} for $\lambda_{SD} = 10^{-1}$ and $\sin\theta = 0.3$. $\Omega^{FO}_{\phi_D}h^2$ is significantly small for all values of λ_{Dh}. Therefore, out of equilibrium decay of ϕ_D can not produce significant number of χ. Due to this, the correct relic density of χ is obtained only through thermal freeze-in production which depends on $Y_{D\chi}$, and not on the coupling λ_{Dh}. Therefore, the required coupling $Y_{D\chi}$ is independent of λ_{Dh}.

- The variation of $Y_{D\chi}$ w.r.t. the variation of λ_{Dh} in figure 12(b) can be understood from figure 7(a). For fixed value of m_{ϕ_D} and m_χ, production of χ through out of equilibrium decay of ϕ_D is proportional to $\Omega^{FO}_{\phi_D}h^2$. As we can see from the green and yellow lines in figure 7(a) that $\Omega^{FO}_{\phi_D}h^2 > 0.12$ but remain constant in the range $10^{-5} < \lambda_{Dh} < 10^{-4}$. For $\lambda_{Dh} > 10^{-4}$, $\Omega^{FO}_{\phi_D}h^2$ increases significantly as λ_{Dh} increases.

This sudden jump occurs due to the cancellation in λ_{H_1}, described earlier. $\Omega^{FO}_{\phi_D} h^2$ again falls much below 0.12 as λ_{Dh} increases further. For a large ϕ_D abundance, the out-of-equilibrium contribution from $\phi_D \to \chi N$ will be substantial. In figure 12(b), for $\lambda_{Dh} > 3 \times 10^{-3}$, due to very suppressed ϕ_D abundance, out of equilibrium decay contribution is small, and the thermal freeze-in contribution alone satisfies the DM abundance. This is represented via the red, yellow and green lines which merge near $\lambda_{Dh} \sim 3 \times 10^{-3}$. For small value of $\lambda_{Dh} < 10^{-4}$, both the out of equilibrium decay of ϕ_D as well as thermal freeze-in production contribute substantially to the relic abundance of χ. In this region, due to the presence of a finite out-of-equilibrium decay contribution, the required value of $Y_{D\chi}$ to satisfy correct DM relic density is typically less when compared to the only thermal freeze-in dominated scenario, represented via the red line. In between $5 \times 10^{-4} < \lambda_{Dh} < 2 \times 10^{-3}$, the ϕ_D abundance is very large due to cancellation in λ_{H_1} leading to a large out-of-equilibrium decay contribution which results in $\Omega_\chi h^2 > 0.12$. Hence, this region is disallowed.

- The magenta line in this figure corresponds to $\lambda_{SD} = 10^{-3}$ and $\sin\theta = 10^{-2}$. The behaviour can again be understood by referring to the magenta line in figure 7(a). $\Omega^{FO}_{\phi_D} h^2$ is much larger than 1.0 for $\lambda_{Dh} < 2 \times 10^{-3}$. This leads to the overproduction of χ via out-of-equilibrium decay of ϕ_D. Hence, the correct relic density of χ in this case is only obtained for λ_{Dh} larger than 2×10^{-3}.

In figure 12(c), we show dependency of $Y_{D\chi}$ on λ_{SD}. The observations are listed as follows:

- For the yellow curve in figure 12(c), the correct relic density of χ is possible to obtain for $\lambda_{SD} > 3 \times 10^{-4}$. For $\lambda_{SD} < 3 \times 10^{-4}$, abundance of ϕ_D is significantly large (see the yellow curve of figure 7(b)), leading to the overproduction of χ via out of equilibrium decay of ϕ_D.

- We can see in figure 7(b) that red, green and blue lines have similar features. The cancellation in λ_{H_1} takes place for different values of λ_{SD}. As we can see the funnel shaped region in figure 12(c) that $Y_{D\chi}$ decreases significantly in the region where cancellation in λ_{H_1} is effective.

In figure 12(d), we show dependence of $Y_{D\chi}$ on $\sin\theta$. The observations are listed as follows:

- The nature of the red, green and blue lines can be understood from figure 7(c). The required value of $Y_{D\chi}$ to satisfy correct DM relic density decreases significantly when ϕ_D abundance gets enhanced. For each of these three lines, in the funnel shaped region, the ϕ_D abundance becomes very large due to the cancellation in λ_{H_1}. This larger ϕ_D abundance leads to $\Omega h^2_\chi > 0.12$, which is ruled out.

- In figure 12(d), the red line represents a scenario, where both the thermal freeze-in production and out-of-equilibrium production of χ can contribute. For $\sin\theta > 0.1$, due to a smaller ϕ_D abundance, mostly thermal freeze-in contribution dominate. Hence a larger value of $Y_{D\chi}$ is required to satisfy the DM relic abundance. In the

JHEP05(2022)182

blue, pink, and green lines, the effect of cancellation in the $\phi_D^\dagger \phi_D H_1$ vertex is clearly visible. For each of these lines, in the funnel shaped region, ϕ_D abundance is very large, leading to an overproduction of χ. For small $\sin\theta$, both the thermal freeze-in and out-of-equilibrium decay can contribute significantly (see figure 7(c)).

4 Collider prospects

This section focuses on the search for the BSM Higgs H_2 via its invisible decay, i.e., $H_2 \to \phi_D^\dagger \phi_D$ at the LHC. The partial decay width for this decay mode is determined by the couplings λ_{SD}. The other production mode of ϕ_D from Z_{BL} is suppressed due to a very heavy Z_{BL}. The possible decay mode of ϕ_D is $\phi_D \to \chi N$ which is controlled by the coupling $Y_{D\chi}$. As mentioned before we assume $Y_{D\chi} = \mathcal{O}(10^{-12})$ to realize the freeze-in production of the DM χ. As a result of this tiny coupling, ϕ_D escapes the detector without leaving any visible footprint. However, its production can be confirmed by the observed imbalance in the transverse momentum. For collider analysis, we consider the mass of ϕ_D to be $m_{\phi_D} = 100\,\text{GeV}$. Other parameters are set to $M_{Z_{BL}} = 7\,\text{TeV}$, $g_{BL} = 0.9$, and $M_N = 50\,\text{GeV}$, which we also consider for the DM study. We first discuss existing constraints on the model parameters from the collider experiment and then project the future sensitivity to probe the coupling λ_{SD} at the HL-LHC.

4.1 LHC constraints

We first discuss the different constraints applicable on the SM-BSM Higgs mixing angle θ, the mass of the BSM Higgs and the quartic coupling λ_{SD}.

Measurement of Higgs signal strength and coupling constant modifiers. The signal strength of SM Higgs decaying into two SM states a, b, such as $WW^*, ZZ^*, \tau\tau, b\bar{b}$, $\mu^+\mu^-$ is,

$$\mu_{H_1 \to ab} = \frac{\sigma(H_1)}{\sigma(H_1)_{\text{SM}}} \frac{\text{BR}(H_1 \to ab)}{\text{BR}(H_1 \to ab)_{\text{SM}}}. \tag{4.1}$$

The global signal strength of H_1 using 139 fb^{-1} data at LHC is measured as $\mu = 1.06 \pm 0.07$ [43]. Due to the presence of the BSM Higgs, which mix with the SM like Higgs states, the standard couplings of the SM Higgs with $W^+W^-, ZZ, \tau\tau$ and others will be modified. We adopt the constant coupling modifiers - κ framework, where κ's are defined as

$$\kappa_x = \frac{\lambda_{xxh}}{\lambda_{xxh}^{SM}} = \cos\theta, \tag{4.2}$$

where λ_{xxh} is the couplings of SM-like Higgs field H_1 with two SM fields in the model considered, and λ_{xxh}^{SM} is the respective coupling in the SM. We consider the ATLAS search [43], and translate the measurements of each measured κ's to the upper limit on the SM and BSM Higgs mixing angle $\sin\theta$. The results are shown in table 4. In our collider analysis for HL-LHC, we adopt a conservative approach and consider relatively smaller values of $\sin\theta = 0.3$, which agrees with the LHC constraints.

JHEP05(2022)182

Parameter	κ_Z	κ_W	κ_t	κ_b	κ_{ta}	κ_g	κ_γ
$\sin\theta$ at 95%CL	0.46	0.45	0.65	0.69	0.65	0.61	0.42

Table 4. Upper limit on $\sin\theta$ obtained from Higgs boson coupling modifiers, $\kappa_{Z/W/t/b/\tau/g/\gamma}$ at 95% CL [43].

SM Higgs decaying to long-lived particle (LLP). The theory under consideration predict several exotic decays of the SM Higgs boson, such as $H_1 \to NN/Z_{BL}\gamma/\phi_D^\dagger\phi_D$,[3] among which $H_1 \to Z_{BL}\gamma/\phi_D^\dagger\phi_D$ are closed kinematically and $H_1 \to NN$ is open having $\mathrm{BR}(H_1 \to NN) = 0.5\%$ for $\sin\theta = 0.3$ and $M_N = 50\,\mathrm{GeV}$. For our benchmark point, decay length of RHN $c\tau_N \simeq 40$ m (for active-sterile mixing, $V \simeq 10^{-7}$) and its possible decay modes are $N \to ljj/\nu jj/ll\nu/3\nu$. Therefore, N is a LLP undergoing displaced decays. The recent CMS search for displaced heavy neutral leptons limits the active-sterile mixing in the mass range 1–18 GeV [44] with the most tight constraint appears $|V|^2 < 10^{-7}$ for $M_N \sim \mathcal{O}(10)\,\mathrm{GeV}$. Our choice of RHN mass $M_N = 50\,\mathrm{GeV}$ and active sterile mixing $V \sim 10^{-7}$ is beyond the range covered in this paper. There are other CMS and ATLAS searches for exotic decays of SM Higgs into two LLP states, which are instead applicable. The CMS and ATLAS have recently searched for exotic decays of the Higgs boson into LLP in the tracking system [45, 46]. These searches are mainly sensitive to LLP with $c\tau = \mathcal{O}(1\,\mathrm{mm}{-}300\,\mathrm{mm})$. Other displaced vertex searches in the tracking system that are also sensitive to Higgs decays to LLP [47, 48]. Our benchmark point is unconstrained from these searches owing to a very long lifetime of the RHN. The latest search for neutral LLP decaying into displaced jets in the ATLAS muon spectrometer [49–51] and in the CMS endcap muon detectors [52] are relevant for LLP with $c\tau \geq \mathcal{O}(1\,\mathrm{m})$. The RHN mostly decays in the muon spectrometer for our benchmark mass point. This is to note that our model prediction of $\mathrm{BR}(H_1 \to NN) = 0.5\%$ for $M_N = 50\,\mathrm{GeV}$ is consistent with the observed bound on BR of Higgs to LLP decay. Note that this constraint is given for the Higgs decaying to scalar LLP and for the two-body decay of the LLP. In reinterpreting this analysis for our scenario, we assume similar signal selection efficiency as given in [52].

Heavy Higgs searches. Other LHC searches [53–57] aimed at probing BSM Higgs via direct measurements can constrain our model. These are the searches to detect a heavy scalar resonance (H_2) decaying into various final states, such as $W^+W^-/ZZ//H_1H_1$. Among them the strongest limits comes from the multi-lepton search in the channel $pp \to H_2 \to ZZ$ [53]. In the model under consideration, H_2 has an additional decay mode $H_2 \to \phi_D^\dagger\phi_D$, which is governed by the coupling λ_{SD}. For large value of the coupling λ_{SD} this decay mode can be dominant over $H_2 \to H_1H_1/W^+W^-/ZZ$. Figure 13(a) shows the contours of $\mathrm{BR}(H_2 \to \phi_D^\dagger\phi_D/W^+W^-/ZZ//H_1H_1/t\bar{t})$ in the M_{H_2} - λ_{SD} plane. The expressions for the respective partial decay widths are given in the appendix. For this plot we fix the scalar mixing angle, $\sin\theta = 0.3$. The gray shaded region represents $\mathrm{BR}(H_2 \to \phi_D^\dagger\phi_D) \geq 0.95$. As $\mathrm{BR}(H_2 \to \phi_D^\dagger\phi_D)$ grows with λ_{SD}, $\mathrm{BR}(H_2 \to ZZ)$ de-

[3]We do not consider the decay chain $H_1 \to \phi_D^\dagger\phi_D(\to \chi N^\star)$ as it is suppressed due to the coupling $Y_{D\chi} < 10^{-10}$.

JHEP05(2022)182

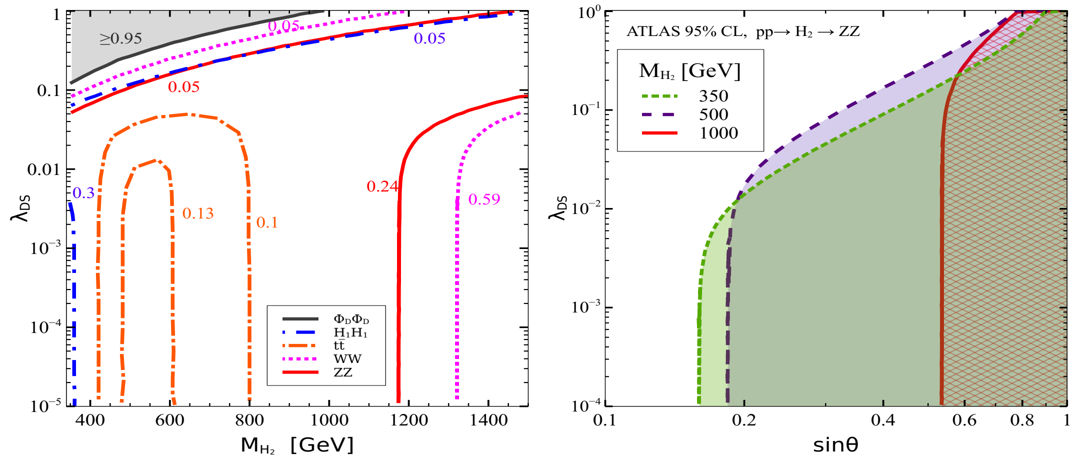

(a) (b)

Figure 13. Figure 13(a): contours of $\mathrm{BR}(H_2 \to \phi_D^\dagger \phi_D/ZZ/W^+W^-/H_1H_1/t\bar{t})$ in M_{H_2} - λ_{SD} plane for $\sin\theta = 0.3$. Figure 13(b): constraints in $\sin\theta - \lambda_{SD}$ plane derived from the ATLAS search for heavy scalar resonance decaying to two Z bosons, $pp \to H_2 \to ZZ \to 4l$ [53].

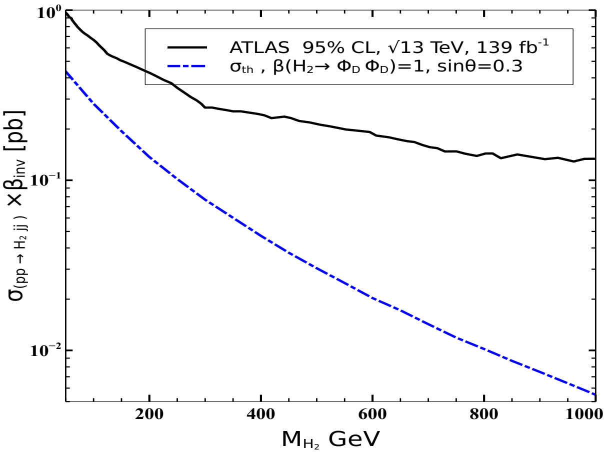

Figure 14. Upper limit on $\sigma(pp \to H_2 jj) \times \mathrm{BR}(H_2 \to \mathrm{inv})$ as a function of M_{H_2} [58], and its comparision with the theory prediction.

creases and hence, the bound on scalar mixing angle $\sin\theta$ becomes weaker for a fixed mass of H_2. This is shown in figure 13(b) for three illustrative mass points of H_2, $M_{H_2} = 350, 500, 1000\,\mathrm{GeV}$. Here we translate the observed limit on $\sigma(pp \to H_2 \to ZZ)$ from ATLAS search [53] into $\sin\theta - \lambda_{SD}$ plane. The shaded regions are disallowed for the respective values of M_{H_2}. For a smaller value of $\lambda_{SD} < 10^{-2}$, for which $H_2 \to ZZ$ branching is significantly larger, a very tight constraint $\sin\theta < 0.2$ appears for $M_{H_2} < 500\,\mathrm{GeV}$.

The CMS and ATLAS collaborations have also performed searches for Higgs boson decaying invisibly. For our parameter choice $H_1 \to \phi_D^\dagger \phi_D$ is closed. Recently ATLAS has searched for such invisible decay of Higgs through vector boson fusion (VBF) production channel and interpreted the result for a heavy scalar particle [58]. In figure 14, the black curve shows the observed bounds on the cross-section times branching ratio to

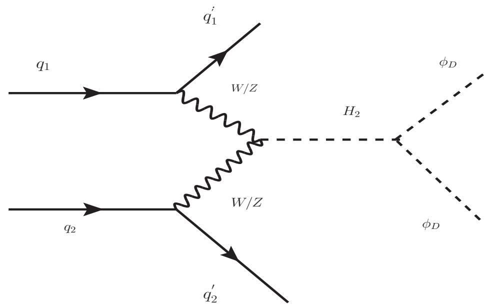

Figure 15. Feynman diagram for the VBF process producing a pair of ϕ_D.

invisible final states of the heavy Higgs from this ATLAS search. The blue-dashed curve represents the theory prediction for $\mathrm{BR}(H_2 \to \mathrm{inv}) = 1$ and for the scalar mixing angle $\sin\theta = 0.3$. In deriving this, we consider a simplistic parton-level analysis with MadGraph5 and do not consider any specific cut-efficiencies. Our theory cross-section agrees with the observed limit in the entire mass range, which is evident from this plot. In the upcoming section, we examined the reach of HL-LHC to search for H_2 decaying invisibly through VBF production mode. The Feynman diagram for this process is shown in figure 15.

4.2 Search for $H_2 \to \phi_D^\dagger \phi_D$ via VBF production mode

The VBF process is one of the most promising channels to search for the invisible decay of Higgs boson [59]. Recently the ATLAS [58] and CMS [60] collaborations have studied the SM Higgs decay to invisible particles and constrained such production processes. Invisible decay of the SM Higgs boson through the VBF channel has been studied for the Higgs portal models [61, 62], for Inert-doublet model [63]. Below, we investigate the production of the BSM scalar H_2 via the VBF process and its subsequent decay to the invisible state ϕ_D. Note that, owing to a very tiny coupling $Y_{D\chi} \sim \mathcal{O}(10^{-12})$, ϕ_D state decays outside the detector.

After gluon-fusion, VBF is the dominant channel for Higgs bosons production at the LHC, characterised by the two highly energetic forward jets [64]. The two VBF jets are widely separated in pseudo-rapidity, lying in the opposite hemisphere of the detector. For the invisible decay $H_2 \to \phi_D^\dagger \phi_D$, the signal is marked by a large transverse momentum imbalance. All these features allow us to discriminate between the signal and background. The dominant SM processes that mimic the signal are $pp \to Z(\to \nu\nu)jj$ and $pp \to W^\pm(\to \nu\ell^\pm)jj$. The latter process contributes when the charged lepton is not detected. QCD multi-jet events with large missing transverse momentum (MET), arising from the mismeasurement of jet energy, can also imitate the VBF signal. A suppressed central jet activity accompanies the VBF signal. On the contrary, QCD jets are more central in the detector. Therefore, the central jet veto and a strong cut on MET could reduce QCD multi-jet events. Another potential background $t\bar{t}$ can be suppressed by vetoing b jets and leptons.

Event simulation. We implement the Lagrangian of this model in FeynRules(v2.3) [65]. The generated UFO files are used in the MC event generator MADGRAPH5(v2.6) [66] to generate the signal events at the leading order. Partonic events are passed through PYTHIA8 [67] to perform showering and hadronization. We implement a cut-count analysis code in CheckMate [68, 69], to calculate the signal and background cut efficiencies. CheckMate makes use of Delphes [70] for the simulation of detector effect, and Fastjet [71, 72] for jet clustering. We use anti-k_t jet clustering algorithm [73] with radius parameter, $R = 0.4$. We estimate the sensitivity of the invisible signature of the H_2 produced via VBF process at the pp-collider, $pp \to H_2 jj \to \phi_D^\dagger \phi_D jj$. Here ϕ_D being a stable particle at the detector length scale gives rise to MET. Thus, the process under consideration leads to $2j + MET$ signature at collider. Among the other SM processes that can fake the signal we simulate the two most dominant processes which are $pp \to Zjj \to \nu\nu jj$ and $pp \to W^\pm jj \to \nu \ell^\pm jj$. We consider the HL-LHC for this study, which is planned to operate with $\sqrt{s} = 14\,\text{TeV}$ and $\mathcal{L} = 3000/\text{fb}$.

Although the signal consists of two jets at the parton level, additional jets can arise due to initial and final state radiation after the parton shower. Thus, we consider up to two extra jets in the final state to simulate backgrounds. During the generation of background events we demand transverse momentum (p_T) of the leading partons: $p_T(j_{1,2}) > 50\,\text{GeV}$, the pseudo-rapidity: $|\eta_j| < 5.0$. We simulate merged sample with 2-4 jets for $W + jets$ and $Z + jets$ using the MLM matching scheme [74]. We consider the parameter xqcut=55 GeV which is the minimum jet measure (p_T/k_T) between partons. Partonic cross-sections for backgrounds $W + jets$ and $Z + jets$ are 528.755×10^3 fb and 223.603×10^3 fb, respectively. Next to leading order (NLO) QCD corrections for $W + jets$ and $Z + jets$ are given in [75], which are negative, and the corresponding K-factors are 0.87 and 0.905 , respectively. We perform the simulation with a harder p_T cut on jets compared to that in the mentioned reference. As, K-factor depends on the kinematic cuts we do not normalise the cross-sections to NLO. For signal we also consider LO cross-section. For $M_{H_2} = (350-1000)\,\text{GeV}$, K-factor varies in the range $1.018 - 0.979$ [76]. The sensitivity can be improved for reduced background cross-sections and enhanced signal cross-section.

Figure 16 shows the normalised distributions of some of the kinematic variables for both signal and background which motivate to design the selection cuts. Figure 16(a) corresponds to the distributions for transverse momentum of the leading jet ($p_T(j_1)$) which shows that the background events possess comparatively harder jets than signal events due to the generation level p_T cut. Figure 16(b) and figure 16(c) represent the difference in pseudo-rapidity ($|\Delta\eta(j_1, j_2)|$) and invariant mass ($M(j_1 j_2)$) of the leading and sub-leading jets. Majority of the signal events hold higher $|\Delta\eta(j_1, j_2)|$ with respect to the background events and hence, larger $M(j_1 j_2)$ as both variables are connected with the equation $M(j_1 j_2) \simeq \sqrt{p_T(j_1)\; p_T(j_2)\; e^{\Delta\eta(j_1,j_2)}}$.[4]

Event selection and results. We closely follow the cuts used in ATLAS search [58], which are as follows

[4]This relation can be derived using the transformation of the four-momentum to p_T, η and ϕ variables.

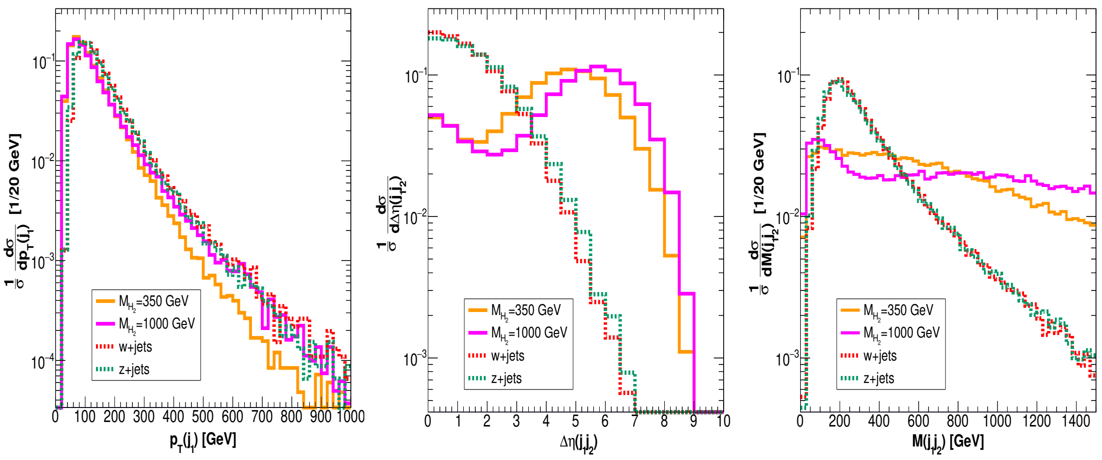

(a) (b) (c)

Figure 16. Normalised Distribution of transverse momentum of the leading jet (figure 16(a)), difference in pseudo-rapidity (figure 16(b)) and invariant mass of the leading and sub-leading jets (figure 16(c)), for both signal and background events. The distributions are without any selection cuts.

- We select events with 2 to 4 jets with $p_T(j) \geq 25\,\text{GeV}$ and $|\eta(j)| < 4.5$, $p_T(j_1) \geq 60\,\text{GeV}$ and $p_T(j_2) \geq 50\,\text{GeV}$.
- We veto events with more than one b-tagged jets.
- We select the events with no lepton and photon candidates. p_T and η requirement for lepton and photon are: $p_T(e) \geq 4.5\,\text{GeV}$, $p_T(\mu) \geq 4\,\text{GeV}$, $p_T(\gamma) \geq 20\,\text{GeV}$, $|\eta(e)| < 2.47$, $|\eta(\mu)| < 2.7$, $|\eta(\gamma)| < 2.37$.
- We demand missing transverse momentum $E_T^{\text{miss}} \geq 150\,\text{GeV}$.
- For the leading and sub-leading jet: $\Delta\phi(j_1, j_2) < 2.0$, $\eta_{j_1} \times \eta_{j_2} < 0$ and $\Delta\eta(j_1, j_2) \geq 3.8$
- The invariant mass of the leading and sub-leading jet: $M(j_1 j_2) \geq 600\,\text{GeV}$.

In table 5, we present the cut efficiencies of the cuts mentioned above for signal and the SM background. We find the lepton veto to be most effective in reducing the $W^\pm + jets$ events. Finally, after the cuts on $\Delta\eta(j_1, j_2)$ and $M(j_1 j_2)$ a significant fraction of both $W^\pm + jets$ and $Z + jets$ events are cut down. The effect of these two cuts is similar as both variables are related.

In the last row, we write the required signal cross-section (in fb) before applying selection cuts to obtain 2σ significance for $\mathcal{L} = 3000/\text{fb}$ luminosity. This is calculated from the relation $\sigma_s = n_\sigma \sqrt{\epsilon_\text{b} \sigma_\text{b}}/(\epsilon_s \sqrt{\mathcal{L}})$, where σ_s (σ_b) is the initial signal (background) cross-section, ϵ_s and ϵ_b is the corresponding cut efficiency, and n_σ is the significance.

In figure 17, we show the HL-LHC prediction for invisible signature of H_2 in $M_{H_2} - \lambda_{SD}$ plane assuming $\sin\theta = 0.3$. The signal significance is calculated for 3000/fb luminosity. The brown solid (brown dashed-dot) line indicates to 2σ (5σ) sensitivity. As per our

	Signal efficiency ϵ_s for M_{H_2}			Background efficiency ϵ_b	
cuts	350 GeV	500 GeV	1000 GeV	$W^{\pm} + jets$	$Z + jets$
$p_T(j_{1,2}) \geq (60, 50)$ GeV	0.38722	0.39005	0.36685	0.77382	0.77113
$n_{b-jet} \leq 1$	0.38552	0.38827	0.36551	0.76276	0.76004
$n_{\ell^{\pm},\gamma} = 0$	0.3382	0.34376	0.32787	0.05173	0.62245
$E_T^{\rm miss} \geq 150$ GeV	0.14735	0.15873	0.15835	0.007814	0.13348
$\Delta\phi(j_1, j_2) < 2.0$	0.1208	0.12989	0.12976	0.002453	0.05685
$\eta_{j_1}.\eta_{j_2} < 0$, $\Delta\eta(j_1, j_2) \geq 3.8$	0.07044	0.08143	0.08923	7.9×10^{-5}	0.00293
$M(j_1 j_2) \geq 600$ GeV	0.06922	0.08042	0.08863	7.3×10^{-5}	0.00290
signal cross-section $\sigma_s = 2\sqrt{\epsilon_b \sigma_b}/(\epsilon_s \sqrt{\mathcal{L}})$ for 2σ significance with $\mathcal{L} = 3000$/fb					
	13.831 fb	11.905 fb	10.802 fb	–	–

Table 5. Cumulative cut efficiencies for Signal: $pp \to H_2 jj \to 2j + MET$ and the SM background: $W + jets$ and $Z + jets$. The numbers in last row are the required signal cross-sections to obtain 2σ significance using 3000/fb luminosity.

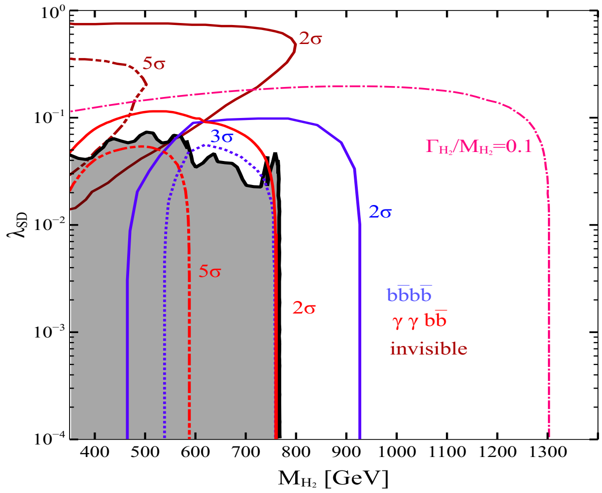

Figure 17. HL-LHC prediction for $pp \to H_2 jj \to jj + MET$, $pp \to H_2 \to H_1 H_1 \to 2b + 2\gamma$ and $pp \to H_2 \to H_1 H_1 \to 4b$ indicated by brown, red and blue color contours in $M_{H_2} - \lambda_{SD}$ plane. Black shaded region is ruled out from the ATLAS search for $H_2 \to ZZ$ [53]. See text for details.

results, 2σ significance can be achieved upto $M_{H_2} \simeq 800$ GeV for λ_{SD} in between 10^{-2} and 1. We also highlighted the region excluded from the ATLAS search for $H_2 \to ZZ$ [53] by the black-shading. As these results are based on narrow width approximation, we show the $\Gamma/M_{H_2} = 0.1$ contour by the pink line. The area enclosed by it corresponds to $\Gamma/M_{H_2} < 0.1$. Note that to obtain the results for the invisible search we take into account the width effect.

The sensitivity of the visible signature of H_2 has been analysed in ref. [77]. Here the authors have considered the production of H_2 via gluon fusion process and subsequent decay to di-Higgs, $pp \to H_2 \to H_1 H_1$. They have studied various final states depending on the decay of SM Higgs H_1 and have shown that $2b+2\gamma$ and $4b$ signatures are more sensitive compared to others. In figure 17, we shows the HL-LHC predictions for di-Higgs channel in $2b + 2\gamma$ and $4b$ final state obtained from the ref. [77]. Here we assume $\sin\theta = 0.3$. For $2b+2\gamma$ signature, regions enclosed by red solid and dashed-dot curves represent 2σ and 5σ sensitivity, respectively. Similarly blue curves show 2σ and 3σ sensitivity for $4b$ final state.

5 Conclusion

We analyse the thermal freeze-in and non-thermal freeze-in production of DM in an extended, gauged $B - L$ model where dark sector fermion χ serves as the DM candidate. In this work, we have a secluded dark sector containing feeble interacting DM candidate χ and a complex scalar field ϕ_D charged under $B - L$ symmetry. The DM fails to thermalise with the surrounding plasma due to suppressed interaction with other bath particles owing to small coupling $Y_{D\chi}$. At an early epoch, it is primarily produced via the decay of ϕ_D via thermal freeze-in mechanism and through the late decay of ϕ_D via the non-thermal freeze-in mechanism. Contrary to the DM field χ, the dark sector scalar field ϕ_D thermalises with the bath particles due to large gauge coupling as well as sizeable interactions with SM and BSM Higgs states. The correct abundance of ϕ_D at decoupling is therefore obtained via the freeze-out mechanism. The annihilation of ϕ_D mediated via Z_{BL}, i.e., $\phi_D^\dagger\phi_D \to Z_{BL} \to f\bar{f}$ etc. decouples from the thermal bath at an earlier epoch compared to the processes mediated via SM and BSM Higgs. The abundance of ϕ_D is hence primarily governed by the interplay of scalar quartic couplings λ_{SD}, λ_{Dh} and SM-BSM Higgs mixing angle $\sin\theta$. For our choice of ϕ_D and χ masses, ϕ_D decaying to χ and RHN is kinematically open, and this is the primary production process for DM. We subdivide the discussion into two scenarios, *Scenario-I*, where the thermal freeze-in via $\phi_D \to \chi N$ contribution is significant, and *Scenario-II*, where the late decay of $\phi_D \to \chi N$ is primarily responsible in satisfying the DM relic abundance. This is to note that the late production of DM through out-of-equilibrium decay of ϕ_D will depend on the abundance of ϕ_D at decoupling obtained through the freeze-out mechanism. Therefore, for suppressed interaction of ϕ_D with the bath particles leading to high abundance of ϕ_D at decoupling significantly enhances the production of χ. We also study mixed scenarios, where the correct relic abundance of χ is governed via both the thermal and non-thermal freeze-in mechanism. We majorly focus our discussion around two benchmark points, 1 and 2. We find that

- Due to relatively large SM-BSM Higgs mixing angle, as well as due to the choice of large quartic couplings λ_{SD}, λ_{Dh}, ϕ_D decouples much later in *Scenario I*, and hence its late decay contributes negligibly to the DM abundance. Here, the primary production of χ occurs due to thermal freeze-in.

- For benchmark 2 (*Scenario II*), the small SM-BSM Higgs mixing and choice of λ_{SD} and λ_{Dh} enables ϕ_D to be out-of-equilibrium in an earlier epoch leading to a larger ϕ_D abundance. In this case, the χ abundance can be built-up primarily from the late decay of ϕ_D.

- We find that for *Scenario-I*, which corresponds to benchmark 1, the dark sector scalar ϕ_D can be produced at a pp collider. This occurs because the SM-BSM Higgs mixing angle is relatively larger to realise this scenario. The ϕ_D is produced from BSM Higgs decay in the VBF channel.

In addition to the detailed DM analysis, we also evaluate the prospect of detection of this model at the HL-LHC. In particular, in section 4, we investigate the possibility of probing the coupling λ_{SD} of ϕ_D with the heavy scalar H_2 at the HL-LHC. This coupling enables an extra decay mode of H_2 to a pair of ϕ_D. When this decay mode becomes dominant, the existing bounds on the mass of H_2 and the scalar mixing angle weaken. To study $H_2 \to \phi_D^\dagger \phi_D$, we consider the production of H_2 from the VBF process, characterised by two forward jets with a large pseudo-rapidity gap. In our case, ϕ_D is stable over the detector length scale resulting in an extra distinguishing feature, the missing transverse momentum. For a fix mass of ϕ_D, we present the 5σ discovery and 2σ exclusion contours in the $M_{H_2} - \lambda_{SD}$ plane. Following a simple cut-count analysis we show that 5σ sensitivity can be obtained for $M_{H_2} \simeq (350-500)$ GeV and λ_{SD} in between 0.03 and 0.35. Similarly, 2σ exclusion limit can be placed for the mass range $\simeq (350-800)$ GeV and for $\lambda_{SD} \simeq (10^{-2}-1)$.

Acknowledgments

MM acknowledges the DST-INSPIRE Research Grant IFA14-PH-99 and research grant from CEFIPRA (Grant no: 6304-2). PB acknowledges SERB CORE Grant CRG/2018/004971 and MATRICS Grant MTR/2020/000668. RP and AR acknowledges SAMKHYA: High-Performance Computing Facility provided by the Institute of Physics (IoP), Bhubaneswar. RP thanks Dr. Shankha Banerjee for useful discussion regarding the collider analysis.

A Analytical expressions of relevant cross-sections and decay widths

We provide the expressions for the relevant cross-sections and decay widths, involved in the coupled Boltzmann equations.

A.1 Decay width of ϕ_D

- $\Gamma(\phi_D \to \chi N) = \frac{y_{D\chi}^2}{8\pi} \frac{m_{\phi_D}^2 - (m_\chi + m_N)^2}{m_{\phi_D}^3} \bar{\lambda}^{\frac{1}{2}}(m_{\phi_D^2}, m_\chi^2, m_N^2)$,
- $\Gamma(\phi_D \to \chi\nu) = \frac{1}{16\pi} \frac{y_{D\chi}^2 y_N^2}{m_N^2} m_{\phi_D} \left(1 - \frac{m_\chi^2}{m_{\phi_D}^2}\right)^2$,

  where in the above, $\bar{\lambda}(x^2, y^2, z^2) = x^2 + y^2 + z^2 - 2xy - 2yz - 2zx$ is a Kälen function.

A.2 Decay width of N

The two body decay width of N_R when m_N is larger than m_W, m_Z and m_{H_1} are as follows,

- $\Gamma(N \to \chi\phi) = \frac{y_{D\chi}^2}{16\pi} \frac{(m_\chi + m_N)^2 - m_{\phi_D}^2}{m_N^3} \bar{\lambda}^{1/2}\left(m_{\phi_D}^2, m_\chi^2, m_N^2\right)$,
- $\Gamma(N \to H_1\nu) = \Gamma(N \to H_1\bar{\nu}) = \frac{y_N^2 m_N}{64\pi} \left(1 - \frac{m_{H_1}^2}{m_N^2}\right)^2$,

- $\Gamma(N \to \ell^- W^+) = \Gamma(N \to \ell^+ W^-) = \frac{y_N^2 m_N}{32\pi}\left(1 - \frac{m_W^2}{m_N^2}\right)^2\left(1 + 2\frac{m_W^2}{m_N^2}\right)$,

- $\Gamma(N \to Z\nu) = \Gamma(N \to Z\bar{\nu}) = \frac{y_N^2 m_N}{64\pi}\left(1 - \frac{m_Z^2}{m_N^2}\right)^2\left(1 + 2\frac{m_Z^2}{m_N^2}\right)$.

For $M_N < m_{W^\pm}, m_Z$, it decays to the three SM fermions through off-shell W, and Z gauge bosons. The three body decay widths are as follows,

$$\Gamma(N \to l_\alpha^- u\bar{d}) = N_c |V_{ud}^{CKM}|^2 |U_\alpha|^2 \frac{G_F^2 M_N^5}{192\pi^3} \mathcal{I}(x_u, x_d, x_l) \tag{A.1}$$

Here, $\mathcal{I}(x_u, x_d, x_l) = 12\int_{(x_d+x_l)^2}^{(1-x_u)^2} \frac{dx}{x}(1 + x_u^2 - x)(x - x_d^2 - x_l^2)\lambda^{\frac{1}{2}}(1, x, x_u^2)\lambda^{\frac{1}{2}}(x, x_l^2, x_d^2)$ and $x_{u/d/l} = \frac{m_{u/d/l}}{M_N}$, $\lambda(a,b,c) = a^2 + b^2 + c^2 - 2ab - 2bc - 2ca$, and $N_c = 3$ is the color factor.

$$\Gamma(N \to l_\alpha^- \nu_\beta l_\beta^+) = |U_\alpha|^2 \frac{G_F^2 M_N^5}{192\pi^3} \mathcal{I}(x_{l_\alpha}, x_{l_\beta}, x_{\nu_\beta}) \tag{A.2}$$

$$\begin{aligned}\Gamma(N \to \nu_\alpha f\bar{f}) = N_c |U_\alpha|^2 \frac{G_F^2 M_N^5}{192\pi^3} \Big[& C_1^f \Big((1 - 14x^2 - 2x^4 - 12x^6)\sqrt{1-4x^2} + 12x^4(x^4-1)L(x) \Big) \\ & + 4C_2^f \Big(x^2(2 + 10x^2 - 12x^4)\sqrt{1-4x^2} + 6x^4(1 - 2x^2 + 2x^4)L(x) \Big) \Big]\end{aligned} \tag{A.3}$$

Here $x = \frac{m_f}{M_N}$, $L(x) = \log\left[\frac{1-3x^2-(1-x^2)\sqrt{1-4x^2}}{x^2(1+\sqrt{1-4x^2})}\right]$. The values of C_1^f and C_2^f are given in [78]

A.3 Cross-cections for relevant processes

Here we give relevant annihilation cross-sections for ϕ_D depletion process are follows,

- $\phi_{\rm D}^\dagger \phi_{\rm D} \to H_1 H_1$

$$\begin{aligned}\lambda_{H_1H_1H_1} &= -3\left[2\,v\lambda_h \cos^3\theta + 2\,v_{BL}\,\lambda_S \sin^3\theta + \lambda_{Sh}\sin\theta\,\cos\theta\,(v\sin\theta + v_{BL}\cos\theta)\right], \\ \lambda_{H_1H_1H_2} &= -\lambda_{Sh}(v_{BL}\cos^3\theta + v\sin^3\theta) + 2v_{BL}(-3\lambda_S + \lambda_{Sh})\cos\theta\sin^2\theta \\ &\quad + 2v(-3\lambda_h + \lambda_{Sh})\cos^2\theta\sin\theta, \\ \lambda_{H_1H_1\phi_{\rm D}^\dagger\phi_{\rm D}} &= -(\lambda_{Dh}\cos^2\theta + \lambda_{SD}\sin^2\theta), \\ M_{H_1H_1} &= \left(\frac{\lambda_{H_1H_1H_1}\lambda_{H_1\phi_{\rm D}^\dagger\phi_{\rm D}}}{(s - m_{H_1}^2) + im_{H_1}\Gamma_{H_1}} + \frac{\lambda_{H_1H_1H_2}\lambda_{H_2\phi_{\rm D}^\dagger\phi_{\rm D}}}{(s - m_{H_2}^2) + im_{H_2}\Gamma_{H_2}}\right) - \lambda_{H_1H_1\phi_{\rm D}^\dagger\phi_{\rm D}}, \\ \sigma_{\phi_D^\dagger\phi_D \to H_1H_1} &= \frac{1}{16\pi s}\sqrt{\frac{s - 4m_{H_1}^2}{s - 4m_{\phi_D}^2}}|M_{H_1H_1}|^2.\end{aligned} \tag{A.4}$$

- $\phi_{\rm D}^\dagger \phi_{\rm D} \to H_2 H_2$

$$
\begin{aligned}
\lambda_{H_2H_2H_2} &= 3\,[2\,v\lambda_h \sin^3\theta - 2\,v_{BL}\lambda_S \cos^3\theta + \lambda_{Sh}\sin\theta\cos\theta\,(v\cos\theta - v_{BL}\sin\theta)]\,,\,,\\
\lambda_{H_2H_2H_1} &= -[6\,v\lambda_h \sin^2\theta\cos\theta + 6\,v_{BL}\lambda_S\cos^2\theta\sin\theta - (2-3\,\sin^2\theta)v_{BL}\lambda_{Sh}\sin\theta,\\
&\quad + (1-3\sin^2\theta)v\lambda_{Sh}\cos\theta]\,,\\
\lambda_{H_2H_2\phi_{\rm D}^\dagger\phi_{\rm D}} &= -(\lambda_{Dh}\sin^2\theta + \lambda_{SD}\cos^2\theta),\\
M_{H_2H_2} &= \left(\frac{\lambda_{H_2H_2H_2}\lambda_{H_2\phi_{\rm D}^\dagger\phi_{\rm D}}}{(s-m_{H_2}^2)+im_{H_2}\Gamma_{H_2}} + \frac{\lambda_{H_2H_2H_1}\lambda_{H_1\phi_{\rm D}^\dagger\phi_{\rm D}}}{(s-m_{H_1}^2)+im_{H_1}\Gamma_{H_1}}\right) - \lambda_{H_2H_2\phi_{\rm D}^\dagger\phi_{\rm D}}\,,\\
\sigma_{\phi_D^\dagger\phi_D\to H_2H_2} &= \frac{1}{16\pi s}\sqrt{\frac{s-4m_{H_2}^2}{s-4m_{\phi_D}^2}}|M_{H_2H_2}|^2.
\end{aligned}
\tag{A.5}
$$

- $\phi_{\rm D}^\dagger \phi_{\rm D} \to W^+W^-$

$$
\begin{aligned}
g_{H_1WW} &= \frac{2m_W^2\cos\theta}{v}\,,\\
g_{H_2WW} &= \frac{2m_W^2\sin\theta}{v},\\
M_{WW} &= \frac{2}{9}\left(1+\frac{(s-2m_W^2)^2}{8m_W^4}\right)\\
&\quad\times\left(\frac{g_{H_1WW}\lambda_{H_1\phi_D^\dagger\phi_D}}{(s-m_{H_1}^2)+im_{H_1}\Gamma_{H_1}} + \frac{g_{H_2WW}\,\lambda_{H_2\phi_D^\dagger\phi_D}}{(s-m_{H_2}^2)+im_{H_2}\Gamma_{H_2}}\right),\\
\sigma_{\phi_{DM}^\dagger\phi_{DM}\to WW} &= \frac{1}{16\pi s}\,\sqrt{\frac{s-4m_W^2}{s-4m_{\phi_D}^2}}|M_{WW}|^2\,.
\end{aligned}
\tag{A.6}
$$

- $\phi_{\rm D}^\dagger \phi_{\rm D} \to ZZ$

$$
\begin{aligned}
g_{H_1ZZ} &= \frac{2m_Z^2\cos\theta}{v}\,,\\
g_{H_2ZZ} &= \frac{2m_Z^2\sin\theta}{v},\\
M_{ZZ} &= \frac{2}{9}\left(1+\frac{(s-2m_Z^2)^2}{8m_Z^4}\right)\\
&\quad\times\left(\frac{g_{H_1ZZ}\lambda_{H_1\phi_D^\dagger\phi_D}}{(s-m_{H_1}^2)+im_{H_1}\Gamma_{H_1}} + \frac{g_{H_2ZZ}\,\lambda_{H_2\phi_D^\dagger\phi_D}}{(s-m_{H_2}^2)+im_{H_2}\Gamma_{H_2}}\right),\\
\sigma_{\phi_{DM}^\dagger\phi_{DM}\to ZZ} &= \frac{1}{16\pi s}\,\sqrt{\frac{s-4m_Z^2}{s-4m_{\phi_D}^2}}|M_{ZZ}|^2\,.
\end{aligned}
\tag{A.7}
$$

- $\phi_{\rm D}^\dagger \phi_{\rm D} \to NN$

$$
\begin{aligned}
\lambda_{H_1 N_R N_R} &= \frac{y_N \sin\theta}{\sqrt{2}} \\
\lambda_{H_2 N_R N_R} &= \frac{y_N \cos\theta}{\sqrt{2}} \\
M_{N_R N_R} &= \frac{\lambda_{H_1 N_R N_R}\ \lambda_{H_1 \phi_D^\dagger \phi_D}}{(s - m_{H_1}^2) + i m_{H_1}\Gamma_{H_1}} + \frac{\lambda_{H_2 N_R N_R}\ \lambda_{H_2 \phi_D^\dagger \phi_D}}{(s - m_{H_2}^2) + i m_{H_2}\Gamma_{H_2}}\,, \\
\sigma_{\phi_D^\dagger \phi_D \to N_R N_R} &= \frac{(s - 4\,m_{N_R}^2)}{32\pi s}\sqrt{\frac{s - 4m_{N_R}^2}{s - 4m_{\phi_D}^2}}\ |M_{N_R N_R}|^2
\end{aligned}
\tag{A.8}
$$

- $\phi_{\rm D}^\dagger \phi_{\rm D} \to f\bar{f}$

$$
\begin{aligned}
\lambda_{H_1 f f} &= \frac{m_f \cos\theta}{v} \\
\lambda_{H_2 f f} &= \frac{m_f \sin\theta}{v} \\
M_{ff} &= \frac{\lambda_{H_1 f f}\ \lambda_{H_1 \phi_D^\dagger \phi_D}}{(s - m_{H_1}^2) + i m_{H_1}\Gamma_{H_1}} + \frac{\lambda_{H_2 f f}\ \lambda_{H_2 \phi_D^\dagger \phi_D}}{(s - m_{H_2}^2) + i m_{H_2}\Gamma_{H_2}}\,, \\
\sigma_{\phi_D^\dagger \phi_D \to f\bar{f}} &= \frac{(s - 4\,m_f^2)}{32\pi s\ n_c}\sqrt{\frac{s - 4m_f^2}{s - 4m_{\phi_D}^2}}\ |M_{ff}|^2
\end{aligned}
\tag{A.9}
$$

In the above, n_c is the color charge and is 1 for leptons and 3 for quarks.

Similarly, the expression of cross-section for the relevant processes in χ production are as follows,

- $\phi_{\rm D}^\dagger \phi_{\rm D} \to \chi\chi$

$$
\begin{aligned}
\sigma = \frac{y_{D\chi}^4}{16\Pi s\left(s - 4M_\phi^2\right)}\Bigg[&-\left(s - 2\left(-M_N^2 + M_\phi^2 + M_\chi^2\right)\right)\left(\log\frac{t_{\rm max} - M_N^2}{t_{\rm min} - M_N^2}\right) \\
&+ \frac{(t_{\rm min} - t_{\rm max})\left(-M_N^2 + (M_\phi - M_\chi)^2\right)\left(-M_N^2 + (M_\phi + M_\chi)^2\right)}{\left(M_N^2 - t_{\rm min}\right)\left(M_N^2 - t_{\rm max}\right)} + t_{\rm min} - t_{\rm max}\Bigg]
\end{aligned}
\tag{A.10}
$$

$t_{\rm min/max} = \mp\frac{\sqrt{s-4M_\phi^2}\sqrt{s-4M_\chi^2}}{2} + M_\phi^2 + M_\chi^2 - \frac{s}{2}$

- $NN \to \chi\chi$

$$
\begin{aligned}
\sigma = \frac{y_{D\chi}^4}{16\Pi s\left(s - 4M_N^2\right)}\Bigg[&\frac{(t_{\rm max} - t_{\rm min})\left((M_N + M_\chi)^2 - M_\phi^2\right)^2}{\left(M_\phi^2 - t_{\rm max}\right)\left(M_\phi^2 - t_{\rm min}\right)} \\
&- 2\left((M_N + M_\chi)^2 - M_\phi^2\right)\log\left(\frac{M_\phi^2 - t_{\rm max}}{M_\phi^2 - t_{\rm min}}\right) + t_{\rm max} - t_{\rm min}\Bigg]
\end{aligned}
\tag{A.11}
$$

$t_{\rm min/max} = -\frac{\sqrt{s-4M_N^2}\sqrt{s-4M_\chi^2}}{2} + M_N^2 + M_\chi^2 - \frac{s}{2}$

- $NH_i \to \chi\phi_D$

$$\sigma = \frac{\lambda^2_{H_i\phi_D\phi_D} y^2_{D\chi}}{32\Pi\left(s-(M_N-M_{H_i})^2\right)\left(s-(M_{H_i}+M_N)^2\right)}\left[\log\left(\frac{M_\phi^2-t_{\min}}{M_\phi^2-t_{\max}}\right)\right.$$
$$\left. - \frac{(t_{\min}-t_{\max})\left((M_N+M_\chi)^2-M_\phi^2\right)}{\left(M_\phi^2-t_{\max}\right)\left(M_\phi^2-t_{\min}\right)}\right] \tag{A.12}$$

$$t_{\min/\max} = \frac{\mp 1}{2s}\sqrt{-2sM_\phi^2-2sM_\chi^2-2M_\phi^2M_\chi^2+M_\phi^4+M_\chi^4+s^2}$$
$$\times\sqrt{-2M_N^2M_{H_i}^2-2sM_{H_i}^2+M_{H_i}^4-2sM_N^2+M_N^4+s^2}$$
$$\frac{-1}{2s}\left(-M_\phi^2+M_\chi^2+s\right)\left(-M_{H_i}^2+M_N^2+s\right)+M_N^2+M_\chi^2 \tag{A.13}$$

References

[1] Planck collaboration, *Planck 2015 results. XIII. Cosmological parameters*, *Astron. Astrophys.* **594** (2016) A13 [arXiv:1502.01589] [INSPIRE].

[2] L.J. Hall, K. Jedamzik, J. March-Russell and S.M. West, *Freeze-In Production of FIMP Dark Matter*, *JHEP* **03** (2010) 080 [arXiv:0911.1120] [INSPIRE].

[3] E. Molinaro, C.E. Yaguna and O. Zapata, *FIMP realization of the scotogenic model*, *JCAP* **07** (2014) 015 [arXiv:1405.1259] [INSPIRE].

[4] A. Biswas, D. Majumdar and P. Roy, *Nonthermal two component dark matter model for Fermi-LAT γ-ray excess and 3.55 keV X-ray line*, *JHEP* **04** (2015) 065 [arXiv:1501.02666] [INSPIRE].

[5] A. Merle and M. Totzauer, *keV Sterile Neutrino Dark Matter from Singlet Scalar Decays: Basic Concepts and Subtle Features*, *JCAP* **06** (2015) 011 [arXiv:1502.01011] [INSPIRE].

[6] B. Shakya, *Sterile Neutrino Dark Matter from Freeze-In*, *Mod. Phys. Lett. A* **31** (2016) 1630005 [arXiv:1512.02751] [INSPIRE].

[7] J. König, A. Merle and M. Totzauer, *keV Sterile Neutrino Dark Matter from Singlet Scalar Decays: The Most General Case*, *JCAP* **11** (2016) 038 [arXiv:1609.01289] [INSPIRE].

[8] A. Biswas and A. Gupta, *Calculation of Momentum Distribution Function of a Non-thermal Fermionic Dark Matter*, *JCAP* **03** (2017) 033 [*Addendum ibid.* **05** (2017) A02] [arXiv:1612.02793] [INSPIRE].

[9] A. Biswas, S. Choubey and S. Khan, *FIMP and Muon $(g-2)$ in a $\mathrm{U}(1)_{L_\mu - L_\tau}$ Model*, *JHEP* **02** (2017) 123 [arXiv:1612.03067] [INSPIRE].

[10] B. Barman and A. Ghoshal, *Scale invariant FIMP miracle*, *JCAP* **03** (2022) 003 [arXiv:2109.03259] [INSPIRE].

[11] T. Hambye, M.H.G. Tytgat, J. Vandecasteele and L. Vanderheyden, *Dark matter direct detection is testing freeze-in*, *Phys. Rev. D* **98** (2018) 075017 [arXiv:1807.05022] [INSPIRE].

[12] P. Bandyopadhyay, E.J. Chun and R. Mandal, *Feeble neutrino portal dark matter at neutrino detectors*, *JCAP* **08** (2020) 019 [arXiv:2005.13933] [INSPIRE].

[13] A. Davidson, *$B-L$ as the fourth color within an* $\mathrm{SU}(2)_L \times \mathrm{U}(1)_R \times \mathrm{U}(1)$ *model*, *Phys. Rev. D* **20** (1979) 776 [INSPIRE].

[14] R.N. Mohapatra and R.E. Marshak, *Local B-L Symmetry of Electroweak Interactions, Majorana Neutrinos and Neutron Oscillations*, *Phys. Rev. Lett.* **44** (1980) 1316 [*Erratum ibid.* **44** (1980) 1643] [INSPIRE].

[15] C. Wetterich, *Neutrino Masses and the Scale of B-L Violation*, *Nucl. Phys. B* **187** (1981) 343 [INSPIRE].

[16] H.M. Georgi, S.L. Glashow and S. Nussinov, *Unconventional Model of Neutrino Masses*, *Nucl. Phys. B* **193** (1981) 297 [INSPIRE].

[17] R.N. Mohapatra and G. Senjanović, *Neutrino Mass and Spontaneous Parity Nonconservation*, *Phys. Rev. Lett.* **44** (1980) 912 [INSPIRE].

[18] P. Minkowski, *$\mu \to e\gamma$ at a Rate of One Out of* 10^9 *Muon Decays?*, *Phys. Lett. B* **67** (1977) 421 [INSPIRE].

[19] P. Bandyopadhyay, E.J. Chun, R. Mandal and F.S. Queiroz, *Scrutinizing Right-Handed Neutrino Portal Dark Matter With Yukawa Effect*, *Phys. Lett. B* **788** (2019) 530 [arXiv:1807.05122] [INSPIRE].

[20] P. Bandyopadhyay, E.J. Chun and R. Mandal, *Implications of right-handed neutrinos in $B-L$ extended standard model with scalar dark matter*, *Phys. Rev. D* **97** (2018) 015001 [arXiv:1707.00874] [INSPIRE].

[21] B.L. Sánchez-Vega, J.C. Montero and E.R. Schmitz, *Complex Scalar DM in a B-L Model*, *Phys. Rev. D* **90** (2014) 055022 [arXiv:1404.5973] [INSPIRE].

[22] S. Singirala, R. Mohanta and S. Patra, *Singlet scalar Dark matter in* $\mathrm{U}(1)_{B-L}$ *models without right-handed neutrinos*, *Eur. Phys. J. Plus* **133** (2018) 477 [arXiv:1704.01107] [INSPIRE].

[23] M. Klasen, F. Lyonnet and F.S. Queiroz, *NLO+NLL collider bounds, Dirac fermion and scalar dark matter in the B-L model*, *Eur. Phys. J. C* **77** (2017) 348 [arXiv:1607.06468] [INSPIRE].

[24] W. Rodejohann and C.E. Yaguna, *Scalar dark matter in the $B-L$ model*, *JCAP* **12** (2015) 032 [arXiv:1509.04036] [INSPIRE].

[25] A. Biswas, S. Choubey and S. Khan, *Neutrino mass, leptogenesis and FIMP dark matter in a* $\mathrm{U}(1)_{B-L}$ *model*, *Eur. Phys. J. C* **77** (2017) 875 [arXiv:1704.00819] [INSPIRE].

[26] T. Basak and T. Mondal, *Constraining Minimal* $\mathrm{U}(1)_{B-L}$ *model from Dark Matter Observations*, *Phys. Rev. D* **89** (2014) 063527 [arXiv:1308.0023] [INSPIRE].

[27] N. Okada and S. Okada, *Z'_{BL} portal dark matter and LHC Run-2 results*, *Phys. Rev. D* **93** (2016) 075003 [arXiv:1601.07526] [INSPIRE].

[28] N. Okada and S. Okada, *Z'-portal right-handed neutrino dark matter in the minimal* $\mathrm{U}(1)_X$ *extended Standard Model*, *Phys. Rev. D* **95** (2017) 035025 [arXiv:1611.02672] [INSPIRE].

[29] K. Kaneta, Z. Kang and H.-S. Lee, *Right-handed neutrino dark matter under the $B-L$ gauge interaction*, *JHEP* **02** (2017) 031 [arXiv:1606.09317] [INSPIRE].

[30] N. Okada and O. Seto, *Higgs portal dark matter in the minimal gauged* $\mathrm{U}(1)_{B-L}$ *model*, *Phys. Rev. D* **82** (2010) 023507 [arXiv:1002.2525] [INSPIRE].

JHEP05(2022)182

[31] N. Okada and Y. Orikasa, *Dark matter in the classically conformal B-L model*, *Phys. Rev. D* **85** (2012) 115006 [arXiv:1202.1405] [INSPIRE].

[32] M. Escudero, N. Rius and V. Sanz, *Sterile Neutrino portal to Dark Matter II: Exact Dark symmetry*, *Eur. Phys. J. C* **77** (2017) 397 [arXiv:1607.02373] [INSPIRE].

[33] M. Becker, *Dark Matter from Freeze-In via the Neutrino Portal*, *Eur. Phys. J. C* **79** (2019) 611 [arXiv:1806.08579] [INSPIRE].

[34] M. Escudero, N. Rius and V. Sanz, *Sterile neutrino portal to Dark Matter I: The* $\mathrm{U}(1)_{B-L}$ *case*, *JHEP* **02** (2017) 045 [arXiv:1606.01258] [INSPIRE].

[35] M. Garny and J. Heisig, *Interplay of super-WIMP and freeze-in production of dark matter*, *Phys. Rev. D* **98** (2018) 095031 [arXiv:1809.10135] [INSPIRE].

[36] L. Covi, J.E. Kim and L. Roszkowski, *Axinos as cold dark matter*, *Phys. Rev. Lett.* **82** (1999) 4180 [hep-ph/9905212] [INSPIRE].

[37] J.L. Feng, A. Rajaraman and F. Takayama, *SuperWIMP dark matter signals from the early universe*, *Phys. Rev. D* **68** (2003) 063504 [hep-ph/0306024] [INSPIRE].

[38] J.L. Feng, A. Rajaraman and F. Takayama, *Superweakly interacting massive particles*, *Phys. Rev. Lett.* **91** (2003) 011302 [hep-ph/0302215] [INSPIRE].

[39] P. Gondolo and G. Gelmini, *Cosmic abundances of stable particles: Improved analysis*, *Nucl. Phys. B* **360** (1991) 145 [INSPIRE].

[40] CMS collaboration, *Search for resonant and nonresonant new phenomena in high-mass dilepton final states at* $\sqrt{s} = 13$ *TeV*, *JHEP* **07** (2021) 208 [arXiv:2103.02708] [INSPIRE].

[41] ATLAS collaboration, *Search for high-mass dilepton resonances using* $139\,fb^{-1}$ *of pp collision data collected at* $\sqrt{s} = 13$ *TeV with the ATLAS detector*, *Phys. Lett. B* **796** (2019) 68 [arXiv:1903.06248] [INSPIRE].

[42] Y. Cheng and W. Liao, *Light dark matter from dark sector decay*, *Phys. Lett. B* **815** (2021) 136118 [arXiv:2012.01875] [INSPIRE].

[43] ATLAS collaboration, *A combination of measurements of Higgs boson production and decay using up to* $139\,fb^{-1}$ *of proton-proton collision data at* $\sqrt{s} = 13$ *TeV collected with the ATLAS experiment*, ATLAS-CONF-2020-027 (2020).

[44] CMS collaboration, *Search for long-lived heavy neutral leptons with displaced vertices in pp collisions at* $\sqrt{s} = 13\,\mathrm{TeV}$ *with the CMS detector*, CMS-PAS-EXO-20-009 (2021).

[45] ATLAS collaboration, *Search for exotic decays of the Higgs boson into long-lived particles in pp collisions at* $\sqrt{s} = 13$ *TeV using displaced vertices in the ATLAS inner detector*, CERN-EP-2021-106 (2021).

[46] CMS collaboration, *Search for Higgs boson decays into long-lived particles in associated* Z *boson production*, CMS-PAS-EXO-20-003 (2021).

[47] CMS collaboration, *Search for long-lived particles decaying to displaced leptons in proton-proton collisions at* $\sqrt{s} = 13\,\mathrm{TeV}$, CMS-PAS-EXO-18-003 (2021).

[48] CMS collaboration, *Search for long-lived particles using displaced jets in proton-proton collisions at* $\sqrt{s} = 13$ *TeV*, *Phys. Rev. D* **104** (2021) 012015 [arXiv:2012.01581] [INSPIRE].

[49] ATLAS collaboration, *Search for events with a pair of displaced vertices from long-lived neutral particles decaying into hadronic jets in the ATLAS muon spectrometer in pp collisions at* $\sqrt{s} = 13$ *TeV*, ATLAS-CONF-2021-032 (2021).

JHEP05(2022)182

[50] ATLAS collaboration, *Search for long-lived neutral particles produced in pp collisions at $\sqrt{s} = 13$ TeV decaying into displaced hadronic jets in the ATLAS inner detector and muon spectrometer*, Phys. Rev. D **101** (2020) 052013 [arXiv:1911.12575] [INSPIRE].

[51] ATLAS collaboration, *Search for long-lived particles produced in pp collisions at $\sqrt{s} = 13$ TeV that decay into displaced hadronic jets in the ATLAS muon spectrometer*, Phys. Rev. D **99** (2019) 052005 [arXiv:1811.07370] [INSPIRE].

[52] CMS collaboration, *Search for Long-Lived Particles Decaying in the CMS End Cap Muon Detectors in Proton-Proton Collisions at $\sqrt{s} = 13$ TeV*, Phys. Rev. Lett. **127** (2021) 261804 [arXiv:2107.04838] [INSPIRE].

[53] ATLAS collaboration, *Search for heavy resonances decaying into a pair of Z bosons in the $\ell^+\ell^-\ell'^+\ell'^-$ and $\ell^+\ell^-\nu\bar{\nu}$ final states using $139\,\mathrm{fb}^{-1}$ of proton-proton collisions at $\sqrt{s} = 13$ TeV with the ATLAS detector*, Eur. Phys. J. C **81** (2021) 332 [arXiv:2009.14791] [INSPIRE].

[54] ATLAS collaboration, *Search for heavy diboson resonances in semileptonic final states in pp collisions at $\sqrt{s} = 13$ TeV with the ATLAS detector*, Eur. Phys. J. C **80** (2020) 1165 [arXiv:2004.14636] [INSPIRE].

[55] ATLAS collaboration, *Combination of searches for Higgs boson pairs in pp collisions at $\sqrt{s} = 13$ TeV with the ATLAS detector*, Phys. Lett. B **800** (2020) 135103 [arXiv:1906.02025] [INSPIRE].

[56] CMS collaboration, *Search for resonant pair production of Higgs bosons decaying to bottom quark-antiquark pairs in proton-proton collisions at* 13 *TeV*, JHEP **08** (2018) 152 [arXiv:1806.03548] [INSPIRE].

[57] ATLAS collaboration, *Search for the $HH \to b\bar{b}b\bar{b}$ process via vector-boson fusion production using proton-proton collisions at $\sqrt{s} = 13$ TeV with the ATLAS detector*, JHEP **07** (2020) 108 [*Erratum ibid.* **01** (2021) 145] [*Erratum ibid.* **05** (2021) 207] [arXiv:2001.05178] [INSPIRE].

[58] ATLAS collaboration, *Search for invisible Higgs boson decays with vector boson fusion signatures with the ATLAS detector using an integrated luminosity of $139\,fb^{-1}$*, ATLAS-CONF-2020-008 (2020).

[59] O.J.P. Eboli and D. Zeppenfeld, *Observing an invisible Higgs boson*, Phys. Lett. B **495** (2000) 147 [hep-ph/0009158] [INSPIRE].

[60] CMS collaboration, *Search for invisible decays of a Higgs boson produced through vector boson fusion in proton-proton collisions at $\sqrt{s} = 13$ TeV*, Phys. Lett. B **793** (2019) 520 [arXiv:1809.05937] [INSPIRE].

[61] N. Craig, H.K. Lou, M. McCullough and A. Thalapillil, *The Higgs Portal Above Threshold*, JHEP **02** (2016) 127 [arXiv:1412.0258] [INSPIRE].

[62] J. Heisig, M. Krämer, E. Madge and A. Mück, *Probing Higgs-portal dark matter with vector-boson fusion*, JHEP **03** (2020) 183 [arXiv:1912.08472] [INSPIRE].

[63] D. Dercks and T. Robens, *Constraining the Inert Doublet Model using Vector Boson Fusion*, Eur. Phys. J. C **79** (2019) 924 [arXiv:1812.07913] [INSPIRE].

[64] R. Kleiss and W.J. Stirling, *Tagging the Higgs*, Phys. Lett. B **200** (1988) 193 [INSPIRE].

[65] A. Alloul, N.D. Christensen, C. Degrande, C. Duhr and B. Fuks, *FeynRules 2.0 — A complete toolbox for tree-level phenomenology*, Comput. Phys. Commun. **185** (2014) 2250 [arXiv:1310.1921] [INSPIRE].

JHEP05(2022)182

[66] J. Alwall et al., *The automated computation of tree-level and next-to-leading order differential cross sections, and their matching to parton shower simulations*, *JHEP* **07** (2014) 079 [arXiv:1405.0301] [INSPIRE].

[67] T. Sjöstrand et al., *An introduction to PYTHIA 8.2*, *Comput. Phys. Commun.* **191** (2015) 159 [arXiv:1410.3012] [INSPIRE].

[68] M. Drees, H. Dreiner, D. Schmeier, J. Tattersall and J.S. Kim, *CheckMATE: Confronting your Favourite New Physics Model with LHC Data*, *Comput. Phys. Commun.* **187** (2015) 227 [arXiv:1312.2591] [INSPIRE].

[69] J.S. Kim, D. Schmeier, J. Tattersall and K. Rolbiecki, *A framework to create customised LHC analyses within CheckMATE*, *Comput. Phys. Commun.* **196** (2015) 535 [arXiv:1503.01123] [INSPIRE].

[70] DELPHES 3 collaboration, *DELPHES 3, A modular framework for fast simulation of a generic collider experiment*, *JHEP* **02** (2014) 057 [arXiv:1307.6346] [INSPIRE].

[71] M. Cacciari, G.P. Salam and G. Soyez, *FastJet User Manual*, *Eur. Phys. J. C* **72** (2012) 1896 [arXiv:1111.6097] [INSPIRE].

[72] M. Cacciari and G.P. Salam, *Dispelling the N^3 myth for the k_t jet-finder*, *Phys. Lett. B* **641** (2006) 57 [hep-ph/0512210] [INSPIRE].

[73] M. Cacciari, G.P. Salam and G. Soyez, *The anti-k_t jet clustering algorithm*, *JHEP* **04** (2008) 063 [arXiv:0802.1189] [INSPIRE].

[74] M. Mangano, *Exploring theoretical systematics in the ME-to-shower MC merging for multijet process*, E-proceedings of Matrix Element/Monte Carlo Tuning Working Group, Fermilab, Chicago, U.S.A. (2002).

[75] J.M. Campbell, R.K. Ellis and D.L. Rainwater, *Next-to-leading order QCD predictions for $W + 2$ jet and $Z + 2$ jet production at the CERN LHC*, *Phys. Rev. D* **68** (2003) 094021 [hep-ph/0308195] [INSPIRE].

[76] P. Bolzoni, F. Maltoni, S.-O. Moch and M. Zaro, *Vector boson fusion at NNLO in QCD: SM Higgs and beyond*, *Phys. Rev. D* **85** (2012) 035002 [arXiv:1109.3717] [INSPIRE].

[77] A. Adhikary, S. Banerjee, R. Kumar Barman and B. Bhattacherjee, *Resonant heavy Higgs searches at the HL-LHC*, *JHEP* **09** (2019) 068 [arXiv:1812.05640] [INSPIRE].

[78] K. Bondarenko, A. Boyarsky, D. Gorbunov and O. Ruchayskiy, *Phenomenology of GeV-scale Heavy Neutral Leptons*, *JHEP* **11** (2018) 032 [arXiv:1805.08567] [INSPIRE].

JHEP05(2022)182